


## Electrical Tuning of Terahertz Plasmonic Crystal Phases

P. Sai<sup>1,\*</sup>, V. V. Korotyeyev<sup>1,2</sup>, M. Dub<sup>1</sup>, M. Słowikowski<sup>1,3</sup>, M. Filipiak<sup>1,3</sup>, D. B. But<sup>1</sup>, Yu. Ivonyak<sup>1</sup>, M. Sakowicz<sup>1</sup>, Yu. M. Lyaschuk<sup>1,2</sup>, S. M. Kukhtaruk<sup>1,2</sup>, G. Cywiński<sup>1</sup>, and W. Knap<sup>1</sup>

<sup>1</sup>*CENTERA Laboratories, Institute of High Pressure Physics PAS, 01-142 Warsaw, Poland*

<sup>2</sup>*V. Ye. Lashkaryov Institute of Semiconductor Physics (ISP), NASU, 03028 Kyiv, Ukraine*

<sup>3</sup>*Centre for Advanced Materials and Technologies, CEZAMAT, Warsaw University of Technology, 02-822 Warsaw, Poland*

 (Received 6 May 2023; revised 16 August 2023; accepted 25 August 2023; published 4 October 2023)

We present an extensive study of resonant two-dimensional (2D) plasmon excitations in grating-gated quantum well heterostructures, which enable an electrical control of periodic charge carrier density profile. Our study combines theoretical and experimental investigations of nanometer-scale AlGaIn/GaN grating-gate structures and reveals that all terahertz (THz) plasmonic resonances in these structures can be explained only within the framework of the plasmonic crystal model. We identify two different plasmonic crystal phases. The first is the *delocalized* phase, where THz radiation is absorbed with the entire grating-gate structure that is realized at a weakly modulated 2D electron gas (2DEG) regime. In the second, the *localized* phase, THz radiation interacts only with the ungated portions of the structure. This phase is achieved by fully depleting the gated regions, resulting in strong modulation. By gate controlling of the modulation degree, we observe a continuous transition between these phases. We also discover that, unexpectedly, the resonant plasma frequencies of ungated parts (in the localized phase) still depend on the gate voltage. We attribute this phenomenon to the specific depletion of the conductive profile in the ungated region of the 2DEG, the so-called edge gating effect. Although we study a specific case of plasmons in AlGaIn/GaN grating-gate structures, our results have a general character and are applicable to any other semiconductor-based plasmonic crystal structures. Our work represents the first demonstration of an electrically tunable transition between different phases of THz plasmonic crystals, which is a crucial step toward a deeper understanding of THz plasma physics and the development of all-electrically tunable devices for THz optoelectronics.

DOI: [10.1103/PhysRevX.13.041003](https://doi.org/10.1103/PhysRevX.13.041003)

Subject Areas: Condensed Matter Physics, Plasmonics

### I. INTRODUCTION

Terahertz (THz) plasmonics [1,2] is a newly emerging field of physics and technology studying the wide class of phenomena relating to the peculiarities of interaction of electromagnetic (*em*) waves of THz frequency range with collective oscillations of electron gas (plasmons) in semiconductor micro- and nanodevices. Generally, two-dimensional (2D) plasmons can be observed in filmlike samples when the scale of electron gas confinement is significantly smaller than the wavelength of the plasmons propagating along the sample. This spatial localization of electron gas oscillations imparts unique physical properties to 2D plasmons that fundamentally differ from those of their bulk counterparts. In the 2D scenario, one of the

most important properties is the ability to tune and manipulate the plasmon parameters through the sample geometry and the electric field. A great interest focuses on the quantum wells (QWs) or 2D material-based structures (including graphene structures), where 2D plasmons can be excited in the ultrathin conductive layer [1–4]. This interest comes from the fact that nanoscale devices using the excitation of the 2D plasma waves are promising for THz optoelectronics detection [4–9] as well as amplification or generation [10–19].

The history of 2D plasmons began more than 50 years ago with the publication of a seminal paper by Chaplik [20] and the subsequent review [21]. These works point out that 2D plasmon frequency  $\omega_p$  exhibits significant wave vector dispersion,  $\omega_p(\mathbf{q})$ , even in the long-wavelength limit, while 3D plasmons are essentially dispersionless. In the retardationless approximation, the electric field associated with the oscillations of 2D plasma waves has two components: longitudinal and transverse. Both components penetrate outside the conductive layer, determining the strong dependence of  $\omega_p(\mathbf{q})$  on the surrounding dielectric or conductive layers.

\*psai@unipress.waw.pl

Published by the American Physical Society under the terms of the [Creative Commons Attribution 4.0 International license](https://creativecommons.org/licenses/by/4.0/). Further distribution of this work must maintain attribution to the author(s) and the published article's title, journal citation, and DOI.

The first experimental observations of 2D plasmon resonances are related to the structures formed by metallic grating gates integrated with silicon inversion layers [22–24]. Later, similar studies were performed for InGaAs/InP [25], AlGaAs/GaAs [26], and AlGaN/GaN [27–31] and, recently, for graphene structures [32,33]. Another promising method for the investigation of 2D plasmons is scanning near-field optical microscopy. This technique is based on the analysis of the near-field images of the electric field or charge distribution and allows for direct observation of effects of plasmonic wave excitation. This attractive method is applied to study the reflection, interference, and damping of the 2D plasmons in graphene [34–37].

The field of 2D plasmonics has seen a surge of interest since the landmark work of Dyakonov and Shur [10] (also, see the recent paper concerning full hydrodynamic simulation of the Dyakonov-Shur plasmon instability effect [38]). Their theoretical predictions show that the steady-state current in the channel of a submicrometer-sized field-effect transistor (FET) can excite large-amplitude plasma oscillations, resulting in the generation of THz radiation with frequency controlled by the gate voltage. An advanced version of plasmonic FETs is the grating-gate structure, in which a periodic charge carrier density profile with intercalated high- and low-density regions is formed. Such structures are known as plasmonic crystals (PCs). Researchers, including Popov, Fateev, and their colleagues [39–42], have extensively studied the THz plasmonic absorption properties of grating-gate-based FETs.

For the case of PC structures, there are several theoretical predictions and experimental attempts [43–49] which denote a possibility to create a solid-state analog of vacuum amplifiers and generators based on the Smith-Purcell effect or related phenomena when a 2D electron beam moving in the periodic potential of the grating can trigger plasmon instability and THz generation. It is expected that semiconductor PC amplifiers and sources can be tuned electrically by the gate voltage (electron density) and/or the lateral current (electron drift velocity). Also, it has been demonstrated recently that 2D plasmon resonance in PC structures is accompanied by a significant phase shift between incident and transmitted waves [50]. This phenomenon has led to the suggestion that an electrical control of this phase shift in grating-gate PC structures [51] could be exploited to create a phased array antenna in the THz range.

Indeed, in the case of PC structure, we deal with large-area millimeter-sized samples, and the whole structure may react as a cascade of thousands of transistors. Therefore, the PC structure can have an advantage over the single FET in terms of the gain values. Additionally, a metallic grating with micron periodicity plays a role of the antenna element that can provide efficient plasmon-THz light coupling and the transformation of 2D plasmon oscillations into electromagnetic waves.

Very important experimental results [52] on graphene PC structures have shown that indeed 2D grating-gate coupled plasmons can open the way toward THz radiation amplifiers. To interpret these results, a simplified analytical model theoretically developed by Kachorovskii and Shur was applied [12]. Despite important theoretical background and the first promising experimental works on grating-gate plasmonic THz sources and amplifiers, the 2D plasmon resonances in PC structures are still not fully understood.

Indeed, comprehensive theoretical and experimental analyses of the resonant plasmon properties of such structures are missing in the literature. This comes from two main reasons.

- (i) *Experimental and technological difficulties.*—THz experiments require systems of millimeter size (the wavelength of 1 THz radiation is approximately 0.3 mm), whereas the typical THz oscillating plasmon cavity is of a few hundred nanometers, which means that in THz experiments one needs samples composed of thousands of gates (grating fingers) with negligible leakage currents (zero defects large surface gate isolation)—to reach the regime of an efficient electrical tuning of plasmon resonances.
- (ii) *Theoretical challenges.*—The grating gate on 2D electron gas (2DEG) forms a nonuniform system composed of intercalated gated and ungated plasmon cavities, for which no analytical solution exists. Theoretical predictions and interpretations require advanced numerical calculations.

In this work, we address these two key issues and conduct both experimental and theoretical investigations of 2D plasmons in grating-gate PC structures based on AlGaN/GaN heterojunctions as a function of the gate-to-channel voltage. We hereby present (i) technology of large surface (a few square millimeters) grating-gate structures with thousands of nanometer gates controlling carrier density (more than two decades) and negligible gate leakage currents (below 100 nA/mm<sup>2</sup>) and (ii) a rigorous electrodynamic approach that enables accurate numerical simulations of the optical characteristics of PCs. This approach is validated through excellent agreement with experimental data, enabling a better understanding of the basic tuning mechanisms of plasmon resonances in PCs. Furthermore, this approach also allows for a comprehensive discussion of existing phenomenological approximations.

In particular, we identify two distinct plasmonic crystal phases: a *delocalized* phase observed at a low carrier density modulation degree and a *localized* phase dominating when the gated part of the 2DEG approaches a total depletion regime (strong modulation). Additionally, we demonstrate an electrically controlled continuous phase transition between these two phases. For experimental studies, we choose grating-gate structures based on AlGaN/GaN heterojunctions. However, our results have

a general character and are applicable to any other semiconductor-based PC structures.

The paper is organized as follows: Section II includes the theoretical model, formalism, and mathematical details of a numerically stable and fast-convergence algorithm developed for the solution of Maxwell's equations. Preliminary calculations of far-field characteristics, particularly transmission coefficients at different modulation degrees of 2DEG, are also presented here. Details of the fabrication, basic characterizations, and THz measurements are collected in Sec. III. The main experimental results and their comparison with electrodynamic simulations of particular PC structures are presented in Sec. IV. Section V is dedicated to detailed analyses of the results based on the calculations of near-field characteristics, particularly, the spatial distribution of  $em$  field and local absorptivity in different PC phases. This section is finalized with conclusions.

## II. ELECTRODYNAMICS OF GRATING-GATE PC STRUCTURES

### A. General consideration

The oscillation frequency of 2D plasma excitation propagated along an infinitely long and the delta-thin conductive layer is given by the following formula [21,41]:

$$\omega_p = \sqrt{\frac{2\pi e^2 n |q|}{m^* \epsilon_{\text{eff}}(q)}}, \quad (1)$$

where  $e$  is the electron charge and  $n$  is the concentration of 2DEG. In this article, all formulas are presented in the centimeter-gram-second system of units. However, when presenting the final results of calculations and measurements, we use the corresponding System International (SI) system units for clarity. This formula is obtained in the hydrodynamic consideration of electron transport (i.e., as a

solution of the eigenvalue problem of the Euler-Poisson system of equations) neglecting the viscosity effect [53] and thermal distribution of electrons in momentum space [16,54]. Also, Eq. (1) assumes a spatially uniform distribution of steady-state electron concentration in the conductive layer and parabolic electron dispersion law with an effective mass  $m^*$ . Effective dielectric permittivity  $\epsilon_{\text{eff}}(q)$  depends on the surrounding of the conductive layer.

In the literature, the two simplest types of 2D plasmons are mainly discussed. The first type is the ungated 2D plasmons, which can be excited in the conductive layer of the QW heterostructure. For these plasmons,

$$\epsilon_{\text{eff}}(q) = \frac{1}{2} \left[ \epsilon_{\text{buf}} + \epsilon_{\text{bar}} \frac{1 + \epsilon_{\text{bar}} \tanh(|q|d)}{\epsilon_{\text{bar}} + \tanh(|q|d)} \right], \quad (2)$$

where  $\epsilon_{\text{buf}}$  and  $\epsilon_{\text{bar}}$  are dielectric constants of a buffer and barrier layers, respectively, and  $d$  is the thickness of the barrier layer [see Fig. 1(b)]. At this, the thickness of the buffer layer is assumed to be much larger than the plasmon wavelength. The second type is the gated 2D plasmons. These plasmons can be excited in the screened QW heterostructure where the barrier layer is covered by a perfect metallic gate. For them,

$$\epsilon_{\text{eff}}(q) = \frac{1}{2} [\epsilon_{\text{buf}} + \epsilon_{\text{bar}} \coth(|q|d)]. \quad (3)$$

If  $|q|d \ll 1$ , then  $\epsilon_{\text{eff}}(q) \approx (\epsilon_{\text{buf}} + 1)/2$  for ungated plasmons and  $\epsilon_{\text{eff}}(q) \approx \epsilon_{\text{bar}}/2|q|d$  for gated ones. As a result, in this limit, ungated plasmons have square-root dispersion  $\omega_O(q)$ , and gated plasmons are described by the linear dispersion  $\omega_G(q)$ :

$$\omega_O = \sqrt{\frac{4\pi e^2 n}{m^* (\epsilon_{\text{buf}} + 1)}} |q|, \quad \omega_G = |q| \sqrt{\frac{4\pi e^2 n d}{m^* \epsilon_{\text{bar}}}}. \quad (4)$$

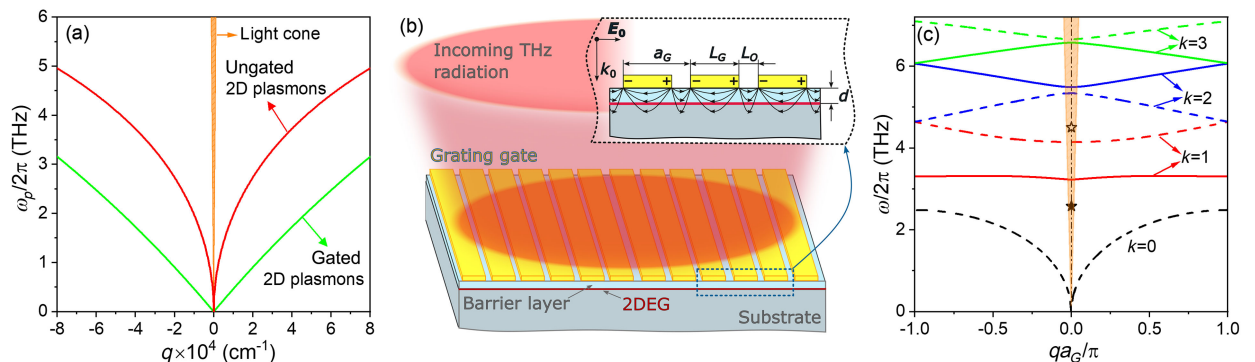


FIG. 1. Dispersions of 2D plasmons given by Eq. (1) for ungated [Eq. (2)] and gated [Eq. (3)] AlGaIn/GaN QW heterostructures with the following parameters:  $n = 10^{13} \text{ cm}^{-2}$ ,  $d = 50 \text{ nm}$ ,  $m^* = 0.2 \times m_e$  ( $m_e$  is the free electron mass), and  $\epsilon_{\text{bar}} = \epsilon_{\text{buf}} = 8.9$  (a); a sketch of the plasmonic crystal structure (b); and the plasmon spectrum under the grating in Brillouin zone-folding representation at  $a_G = 1 \mu\text{m}$ ,  $f = 0.4$ , and the same other parameters (c). These results are obtained in the electrostatic limit, using the algorithm in Ref. [39]. Stars indicate the resonant frequencies of gated (star) and ungated (open star) plasmons calculated from Eq. (1) at  $q = 2\pi/a_G$ .

Remarkably, for typical parameters of QW heterostructures, characteristic frequencies of both types of 2D plasmons belong to the THz frequency range at the micron and submicron scale of their wavelengths,  $\lambda_p = 2\pi/|q|$ . The latter is illustrated in Fig. 1(a). Also, it is seen that the gated plasmons have smaller phase velocity than ungated plasmons.

It should be noted that 2D plasmons, as well as other classes of surface *em* waves, such as surface plasmon polaritons [55] or surface phonon polaritons [56], cannot be directly excited by incident *em* radiation. The 2D plasmon-photon interaction in the laterally uniform sample is forbidden, because the wave vector of 2D plasmons is much greater than the wave vector of the incident radiation [see the light cone in Fig. 1(a)] at a given frequency; i.e., it is impossible to satisfy energy and momentum conservation laws simultaneously.

In order to provide an effective coupling between the 2D plasmons and *em* waves, the electron conductive channel should be supplemented by a lateral microstructure of the sample (plasmonic structure), for example, by using a subwavelength metallic grating [Fig. 1(b)]. Such a grating, formed by long metallic strips, plays the role of a broadband antenna that can effectively couple incident radiation with plasmon oscillations of 2DEG, as well as a polarizer for incident THz radiation and a concentrator of *em* energy in the near field [57,58].

In the framework of the simple physical interpretation, the incoming THz wave with *p* polarization (electric field is oriented perpendicularly to the grating strips) induces instantaneous dipoles (electrical vibrators) at the edges of the strips. In turn, these dipoles excite the particular 2D plasmons. The efficiency of such coupling and selection of the resonant plasmonic mode is controlled by the grating geometry—grating period  $a_G$  and grating filling factor  $f = L_G/a_G$ —as well as by the thickness of the barrier layer  $d$ .

On the other hand, the interaction of the incident wave with metallic grating stipulates the formation of the strongly nonuniform distribution of the *em* field (near field) in the proximity of the grating coupler. For the actual case of subwavelength grating, the near field is composed of  $k$  evanescent ( $k = 1, 2, 3, \dots$ ) waves and one propagating ( $k = 0$ ) wave. Evanescent waves decay exponentially away from the grating plane approximately  $\exp(-2\pi kz/a_G)$  with the periodicity in the lateral direction. The evanescent waves with in-plane wave vector  $q = 2\pi k/a_G$  excite plasmons of different  $k$  orders when the frequency of the incident THz wave coincides with the frequency of a particular eigenplasmon mode of 2DEG under the grating. As a result, part of *em* energy transfers to the electron subsystem, and resonant absorption of incident radiation occurs.

More rigorously, the presence of the metallic grating leads to the “folding” and splitting of plasmon dispersion

branches [see Fig. 1(c)]. As seen, in Brillouin zone-folding representation [14,59], the 2D plasmon spectrum consists of a set of branches. Therefore, such a plasmonic structure can be called a plasmonic crystal (PC). At small  $q$ , the branches marked by solid lines in Fig. 1(c) become optically active, and they can interact with *em* waves. The dashed lines represent the *dark* plasmon modes. Because of the symmetry of the electric field oscillations, they do not interact with *em* waves [39]. The resonant frequencies of the PC structure (calculated for  $f = 0.4$ ) are defined by intersections of plasmonic branches with the light cone. The symbols (stars) in Fig. 1(c) show the fundamental ( $k = 1$ ) frequencies of pure gated (solid star) and ungated (open star) plasmons calculated using Eq. (1) at grating wave number  $2\pi/a_G$ . They correspond to the two limiting cases of narrow-slit grating ( $f \rightarrow 1$ ) and wide-slit grating ( $f \rightarrow 0$ ). The fact that the stars are not lying on any dispersion curve near  $k = 0$  illustrates the inapplicability of a single-mode approximation for a correct description of the resonant frequencies of any realistic PC structure ( $0 < f < 1$ ).

## B. Electrodynamic simulations

The response of the grating-gate PC structures to THz radiation is analyzed by the rigorous electrodynamic simulations based on numerical solutions of Maxwell’s equations in the framework of the integral equation (IE) method following the pioneering work of Ref. [40]. Generally, this technique uses Green function formalism and is based on a reduction of Maxwell’s system of equations to the linear IEs in the coordinate space. The latter can be solved, for example, using Galerkin schemes. In contrast to well-known and widely applied Fourier-modal methods [60,61], the IE technique provides much faster and guaranteed convergence of the results with a given accuracy.

In general, the PC structure can be considered as a multilayer semiconductor heterostructure with 2DEG conducting channel integrated with metal grating. The geometry of such a structure is sketched in Fig. 2. In this work, the IE method in Ref. [40] is generalized to be valid for arbitrary geometries of the metal grating and the semiconductor heterostructures. This modification takes into account different forms of the spatial profiles of 2DEG conductivity and the possibility of incline incidence of electromagnetic waves. As is shown in Fig. 2, the considered PC structure consists of the  $N - 1$  layers placed between  $N$  interfaces. Each layer is described by dielectric permittivity,  $\epsilon_{r=1\dots N-1}$  (where subscript  $r$  numerates here different layers of the structure). The whole structure is placed between two dielectric half-spaces with  $\epsilon_0$  and  $\epsilon_N$ . The periodic metallic grating is deposited on the top of the first layer ( $z = z_0$ ). The grating is characterized by the grating period  $a_G$ , the gate finger width  $L_G$ , and the grating opening width  $L_O$ . Such grating is formed by infinitely

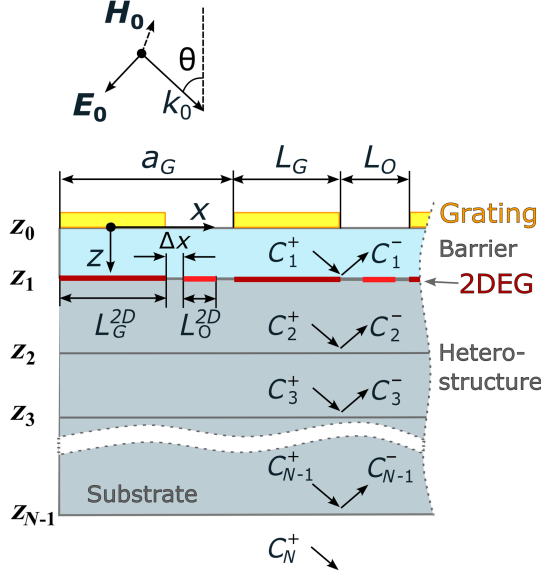


FIG. 2. Sketch of the considered plasmonic structure.

long (along the  $y$  axis) parallel strips of the metal with 2D conductivity,  $\sigma_M$ . The spatial profile of the grating conductivity  $\sigma^G(x)$  is taken as follows:

$$\sigma^G(x) = \begin{cases} \sigma_M v_G(x), & -\frac{L_G}{2} < x < \frac{L_G}{2} \\ 0, & \frac{L_G}{2} < x < a_G - \frac{L_G}{2}, \end{cases} \quad (5)$$

where both metallic grating and 2DEG are assumed as delta thin. The 2DEG conductive layer has the coordinate  $z = z_1$ , and it is described by the 2D conductivity  $\sigma^{2D}(x)$  with the following spatial profile:

$$\sigma^{2D}(x) = \begin{cases} \sigma_{G,O}^{2D} v_G^{2D}(x), & -\frac{L_G^{2D}}{2} < x < \frac{L_G^{2D}}{2} \\ \sigma_O^{2D} v_O^{2D}(x), & \frac{L_G^{2D}}{2} + \Delta x < x < a_G - \frac{L_G^{2D}}{2} - \Delta x, \end{cases} \quad (6)$$

where  $\sigma_{G,O}^{2D} = e\mu_{G,O}n_{G,O}$  and  $v_G(x)$ ,  $v_G^{2D}(x)$ ,  $v_O^{2D}(x)$  are dimensionless conductivity profiles of the metallic grating strips and gated and ungated regions of the 2DEG, respectively. Under applied gate voltage  $V_G$ , the concentrations  $n_G$  and  $n_O$  can be essentially different. Also, we introduce the parameter  $\Delta x$ , which describes the effective width of the ungated region of 2DEG,  $L_O^{2D} = a_G - L_G^{2D} - 2\Delta x$  (note the method in Ref. [40] was developed only for the case of  $\Delta x = 0$ ). This approach accounts for the fact that the depletion region under the gate extends laterally beyond the geometrical gate finger dimension.

We suppose that the whole structure is uniformly illuminated by the plane  $em$  wave at the incidence angle,  $\theta$ , having TM polarization; i.e., the  $x$  component of the electric field  $E_{0,x}$  orients perpendicularly to the

grating strips. At this, the electric field of the  $em$  wave induces in the grating strips instantaneous dipoles (see, for example, Ref. [58]) which form a spatially inhomogeneous field in the near-field zone. This field can effectively excite the plasmon oscillations in 2DEG.

In such geometry, the nonzero components of the  $em$  wave are  $E_x$ ,  $E_z$ , and  $H_y$ . The master equation for the electric components  $E(\mathbf{r}, t)$  of the  $em$  field which is a result of the interaction of incident wave with plasmonic structure is

$$\text{rot rot} \mathbf{E}(\mathbf{r}, t) + \frac{\epsilon(\mathbf{r})}{c^2} \frac{\partial^2 \mathbf{E}(\mathbf{r}, t)}{\partial t^2} = -\frac{4\pi}{c^2} \frac{\partial \mathbf{j}(\mathbf{r}, t)}{\partial t}. \quad (7)$$

Here, the term of the displacement current contains dielectric permittivity  $\epsilon(\mathbf{r})$  which is a steplike function and constant within each medium. Conduction current includes the current density in the metallic grating,  $\mathbf{j}^G(\mathbf{r}, t)$ , and in the 2DEG conduction layer,  $\mathbf{j}^{2D}(\mathbf{r}, t)$ . In the delta-thin treatment of both currents,

$$j_x(\mathbf{r}, t) = j^G(x, t)\delta(z - z_0) + j^{2D}(x, t)\delta(z - z_1), \quad (8)$$

where  $\delta$  denotes the Dirac delta function. Because of the periodicity of the plasmonic structure, we can introduce the spatial Fourier transform of the electric field and the currents with respect to the  $x$  coordinate:

$$\begin{bmatrix} E_{\{x,z\}}(\mathbf{r}, t) \\ j^G(x, t) \\ j^{2D}(x, t) \end{bmatrix} = \sum_{k=-\infty}^{+\infty} \begin{bmatrix} E_{\{x,z\},\omega,k}(z) \\ j_{\omega,k}^G \\ j_{\omega,k}^{2D} \end{bmatrix} \exp(i[Q_k x - \omega t]). \quad (9)$$

In Eq. (9), we assume harmonic temporal dependencies of  $em$  wave with angular frequency  $\omega$ . Periodicity parameter  $Q_k = q_k + k_0\sqrt{\epsilon_0} \sin \theta$  ( $q_k = 2\pi k/a_G$  and  $k_0 = \omega/c$ ). Now, the wave equation (7) can be transformed to the system of the differential equations with respect to the  $z$  coordinate for each  $k$ -spatial Fourier harmonics of the  $x$  component of the electric field in every  $r$ th medium ( $r = 0 \dots N$ ). So for  $E_{x,\omega,k}$  we obtain

$$\frac{d^2 E_{x,\omega,k}^{(r)}}{dz^2} - \lambda_{r,k}^2 E_{x,\omega,k}^{(r)} = \frac{4\pi i \lambda_{r,k}^2}{\epsilon_r \omega} \left[ j_{\omega,k}^G \delta(z - z_0) + j_{\omega,k}^{2D} \delta(z - z_1) \right], \quad (10)$$

where the characteristic parameter

$$\lambda_{r,k} = \begin{cases} \sqrt{Q_k^2 - \epsilon_r k_0^2}, & Q_k > \text{Re}[\sqrt{\epsilon_r} k_0] \\ -i\sqrt{\epsilon_r k_0^2 - Q_k^2}, & Q_k < \text{Re}[\sqrt{\epsilon_r} k_0] \end{cases} \quad (11)$$

describes the spatial localization of the  $k$ -spatial Fourier harmonic. In Eq. (11), the upper line corresponds to evanescent modes and the lower line corresponds to propagated modes. For the actual case of deeply subwavelength grating, optical characteristics of the structure,

such as transmission and reflection coefficients, are formed by the single propagated mode with  $k = 0$ .

The formal solutions of system (10) can be presented as a superposition of transmitted (“+”) and reflected (“−”) waves and one reads as

$$E_{x,\omega,k}^{(r)} = \begin{cases} C_{0,k}^+ \exp(-\lambda_{0,k}z) + C_{0,k}^- \exp(\lambda_{0,k}z), & z < z_0 \\ \vdots \\ C_{r,k}^+ \exp[-\lambda_{r,k}(z - z_{r-1})] + C_{r,k}^- \exp[\lambda_{r,k}(z - z_r)], & z_{r-1} \leq z \leq z_r \\ \vdots \\ C_{N,k}^+ \exp[-\lambda_{N,k}(z - z_{N-1})], & z \geq z_{N-1}. \end{cases} \quad (12)$$

This system should be supplemented by the following boundary conditions at the  $r$ th interface:

$$E_{x,\omega,k}^{(r)} \Big|_{z=z_r} = E_{x,\omega,k}^{(r+1)} \Big|_{z=z_r}, \quad (13)$$

$$\begin{aligned} & \frac{\epsilon_{r+1}}{\lambda_{r+1,k}^2} \frac{dE_{x,\omega,k}^{(r+1)}}{dz} \Big|_{z=z_r} - \frac{\epsilon_r}{\lambda_{r,k}^2} \frac{dE_{x,\omega,k}^{(r)}}{dz} \Big|_{z=z_r} \\ &= \frac{4\pi i}{\omega} \left[ j_{\omega,k}^G \delta_{r,0} + j_{\omega,k}^{2D} \delta_{r,1} \right]. \end{aligned} \quad (14)$$

Here,  $\delta_{r,r'}$  is the Kronecker delta symbol. Equation (13) corresponds to the continuity of the tangential components of the electric fields, and the latter Eq. (14) takes into account the discontinuity of the tangential component of the magnetic field due to the presence of the delta-thin conductive layers. Without loss of generality, we can put that  $C_{0,k}^+ = \delta_{k,0} E_{0,x}$ , where  $E_{0,x} = E_0 \cos \theta$  and  $E_0$  is the electric field amplitude of the incident wave.

After some algebraic transformations, we can come to the relationships between Fourier harmonics of the  $x$  component of the electric fields in the plane of the metallic grating ( $z = z_0$ ) and 2DEG conductive layer ( $z = z_1$ ) and Fourier harmonics of the corresponding currents:

$$\begin{aligned} E_{\omega,k}^G &= -\frac{2\pi i}{c\sqrt{\epsilon_0}} \left[ Z_{\omega,k}^{(11)} j_{\omega,k}^G + Z_{\omega,k}^{(12)} j_{\omega,k}^{2D} \right] + \eta_{\omega,k}^{(1)} \delta_{k,0} E_{0,x}, \\ E_{\omega,k}^{2D} &= -\frac{2\pi i}{c\sqrt{\epsilon_0}} \left[ Z_{\omega,k}^{(21)} j_{\omega,k}^G + Z_{\omega,k}^{(22)} j_{\omega,k}^{2D} \right] + \eta_{\omega,k}^{(2)} \delta_{k,0} E_{0,x}. \end{aligned} \quad (15)$$

Here,  $E_{\omega,k}^{G,2D}$  are  $E_{x,\omega,k}^{(1)}(z_0)$  and  $E_{x,\omega,k}^{(2)}(z_1)$ , respectively. The explicit form of the introduced parameters is specified in Supplemental Material [62].

In the frameworks of the IE method, the system (15) should be transformed into coordinate space and formulated as a system of three linear integral equations with

respect to currents  $j^G(x)$ ,  $j_G^{2D}(x)$ , and  $j_O^{2D}(x)$  induced by the  $em$  wave in the grating strip and gated and ungated regions of 2DEG, respectively. For this, it is necessary to multiply both sides of the system (15) by  $\exp(iQ_k x)$  and then sum them over all  $k$ , taking into account local approximation for the currents:

$$j^{G,2D}(x) = \sigma^{G,2D}(x) E^{G,2D}(x). \quad (16)$$

The mathematical details of this procedure, including the method of solution for the obtained IEs and the final formulas used for calculating the transmission, reflection, and absorption spectra (including near-field patterns), are provided in Supplemental Material [62]. In Supplemental Material [62], we also discuss the convergence of the developed method and compare it with another purely numerical scheme based on finite-element calculations. We utilize the described numerical scheme to investigate the main peculiarities of the THz transmission spectra of the PC structures described below, at different applied gate voltages.

### C. Gate-voltage-tuned plasmonic spectra

In order to describe the different phases of the plasmonic crystals, we introduce the dimensionless parameter that characterizes the modulation degree,  $\rho$ . It is defined as  $\rho(V_G) = [n_O - n_G(V_G)]/[n_O + n_G(V_G)]$ , where  $n_O$  and  $n_G$  are concentrations of 2DEG in ungated and gated regions of 2DEG, respectively. The  $n_G(V_G)$  can be controlled by the applied gate voltage  $V_G$ . For the case of the uniform spatial profile,  $n_O = n_G$ , and  $\rho = 0$ . For the case when  $|V_G|$  is larger than the threshold voltage  $|V_{th}|$ ,  $\rho \sim 1$ . In the latter case, the space between the drain and source is divided into highly conductive ungated regions and almost depleted gated regions. As shown below, the resonant peculiarities of the transmission spectra strongly depend on modulation degree  $\rho(V_G)$ .

TABLE I. AlGaIn/GaN heterostructure parameters.

Layer from the top	Thickness	Permittivity	Ref.
GaN cap layer	2.4 nm	8.9	[63]
Al <sub>0.25</sub> Ga <sub>0.75</sub> N	20.5 nm	8.9	[63]
GaN	255 nm	8.9	[63]
AlN	62 nm	8.5	[63]
SiC	500 $\mu$ m	9.7	[64]

First, we imply that conductivity profiles of the metallic grating and 2DEG have an abrupt steplike form, i.e.,  $v_G(x) = v_G^{2D}(x) = v_O^{2D}(x) = 1$ , and the width of the gated region of 2DEG coincides with the grating-finger width,  $L_G^{2D} = L_G$ .

In calculations, we use the parameters of the typical GaN-based high electron mobility heterostructure used in the experiment (see Sec. III). The whole structure consists of four bulklike dielectric layers: AlGaIn barrier layer with thickness  $d_1 = 23$  nm and GaN buffer layer with  $d_2 = 255$  nm placed directly on AlN nuclear layer with  $d_3 = 62$  nm (see Table I in Sec. III). In order to avoid the emergence of the Fabry-Pérot fringes, here, we consider a membranelike SiC substrate with a thickness  $d_4 = 1$   $\mu$ m.

For the 2DEG densities, we assume the linear dependence of  $n_G(V_G)$  provided by so-called gradual channel approximation:

$$n_G = \begin{cases} \frac{\epsilon_1 V_0}{4\pi e d_1}, & \text{at } V_0 \geq 0, \\ 0, & \text{at } V_0 < 0, \end{cases} \quad (17)$$

where  $V_0 = V_G - V_{th}$  is the gate voltage swing and  $V_{th}$  is the threshold voltage of channel depletion. At this, we set that  $n_O$  is a constant and equal to  $9 \times 10^{12}$  cm<sup>-2</sup>, threshold voltage  $V_{th} = -2.9 \pm 0.3$  V, and  $\epsilon_1 = 8.9$  (see Sec. III).

The metallic grating is assumed to be gold and delta thin with 1.5  $\mu$ m period, grating filling factor  $f = 0.6$ , and dispersionless 2D conductivity  $\sigma^M = 2 \times 10^{12}$  cm/s (or 2.2 S in SI units). It corresponds to the bulk conductivity of  $4 \times 10^{17}$  s<sup>-1</sup> (or  $4.5 \times 10^7$  S/m in SI units) and the grating thickness of 50 nm.

High-frequency mobilities of 2DEG in the gated and ungated regions are assumed to be equal,  $\mu_G = \mu_O$ , and both obey the Drude-Lorentz model,  $\mu_{G,O} = \mu/(1 - i2\pi\nu\tau)$  with frequency  $\nu$  and effective scattering time  $\tau = \mu m^*/e$ . Here, we set  $\mu = 7500$  cm<sup>2</sup>/V s that corresponds to the scattering time  $\tau = 0.85$  ps at electron effective mass in GaN,  $m^* = 0.2 \times m_e$ . All calculations are performed at normal incidence,  $\theta = 0$ . The cryogenic temperature mobility (scattering time) in the case of GaN structure on SiC substrates used in our experiments is mainly determined by two quasielastic scattering mechanisms: electron-acoustic phonons and electron-dislocation scattering [65–67].

It should be noted that the applicability of the used Drude-Lorentz model for the high-frequency response of degenerate 2DEG at low temperatures and frequencies larger than 0.5 THz was recently discussed in Ref. [68] for the case of nitride heterostructures. In the mentioned paper, the kinetic theory of small-signal conductivity was developed neglecting electron-electron ( $e-e$ ) scattering. Our estimations (according to Ref. [69]) of the  $e-e$  scattering rate,  $\gamma_{e-e}$ , performed at an electron temperature of 10 K and electron concentration of  $6 \times 10^{12}$  cm<sup>-2</sup>, provide the value of approximately  $10^{11}$  s<sup>-1</sup>, which is an order of magnitude smaller than the scattering rate  $\gamma_e = 1/\tau \sim 10^{12}$  s<sup>-1</sup>, corresponding to the contribution of other scattering mechanisms. Therefore, we neglect  $e-e$  scattering in our theoretical model.

Figure 3(a) demonstrates the calculated contour plot of the transmittance in the plane “gate voltage swing–frequency” in the wide frequency range of 0.1–7 THz.

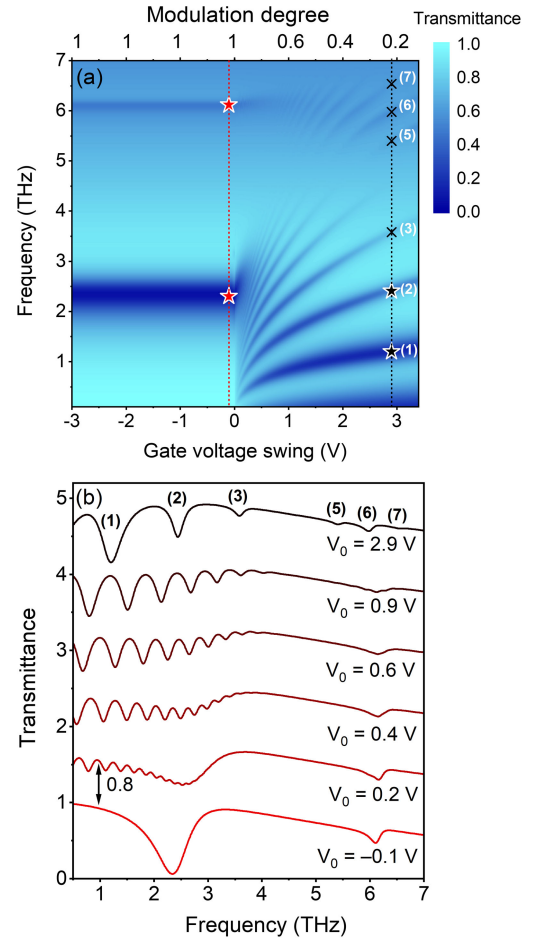


FIG. 3. Calculated contour plot of the transmittance in the plane  $V_0 - \nu$  (a). Transmittance as a function of the frequency as a function of the gate voltage swing (V) (b). Vertical dashed lines in (a) show the gate voltage swing values 2.9 and  $-0.1$  V for plots in (b). The fundamental resonance “(1)” and visible high-order resonances “(2),” “(3),” “(5),” “(6),” and “(7)” are marked at  $V_0 = 2.9$  V. Stars in (a) mark the points for the near-field simulations to be discussed in Sec. V.

One can clearly see two different regions (below and above the threshold voltage) that we attribute to two different plasmonic crystal phases. In the first one, above-threshold voltage  $V_0 > 0$ , the transmission spectra possess multiple resonances that are tuned by the gate voltage and can be attributed to the resonant excitation of 2D plasmons of different orders in 2DEG with a spatially modulated profile of electron concentration. In the frequency range of 0.1–4 THz, we can identify the most intensive first-order and less intensive second- and third-order plasmon resonances [see transmittance spectra in Fig. 3(b) for  $V_0 = 2.9$  V].

With the decrease of  $V_0$  (an increase in modulation degree), these resonances are redshifted, and the resonances of a higher order appear to show even up to six resonances as is seen in the transmittance spectra for  $V_0 = 0.9$  V in Fig. 3(b). At  $V_0 = 0.6$  V [see Fig. 3(b)], the transmittance exhibits a multiresonant structure, and we can talk about the formation of the quasicontinuous plasmonic bands.

With even further gate voltage swing decrease, one can observe a gradual transition to the second plasmonic crystal phase with gate-voltage-independent modes. This transition is clearly seen in the swing voltage range of 0.4–0 V [see curves in Fig. 3(b) calculated for  $V_0 = 0.4$  V and  $V_0 = 0.2$  V], where the specific evolution of THz transmission spectra with initialization of the formation of single resonant mode regime in the frequency range of 0.1–4 THz occurs. At negative swing voltages, the carrier density under the gated regions is negligible, and, therefore, this mode corresponds to the resonant excitation of the plasma oscillations in the limiting case of electrically formed 2DEG-strip grating [11,70,71].

As we show later, while the phase of PC above the threshold voltage ( $V_0 > 0$ ) is characterized by *em* energy absorption, in both the gated and ungated regions, in the phase at  $V_0 < 0$  *em* energy is absorbed only in ungated regions. Therefore, we call these phases delocalized and localized ones, respectively.

The contour plot in Fig. 3(a) illustrates the phase transition scenario between different PC phases. When the applied voltage exceeds the threshold value ( $V_0 > 0$ ), PC exhibits a well-developed delocalized phase. In this phase, multiple resonances appear in the transmission spectra, corresponding to various orders of 2D plasmon excitations. As the voltage approaches  $V_0 \sim 0$ , the transition from the delocalized phase to the localized phase of PC begins. During this transition, the multiresonant structure in the transmission spectra disappears, particularly within the frequency range of 4–5 THz, where none of the plasmon resonances exist. The higher-order resonances in the delocalized phase that are resonant with localized plasmons getting stronger. This effect is clearly observed around 2.4 and 6.2 THz. Eventually, these higher-order resonances transform into strong plasmon resonances in the localized phase of PC.

### III. EXPERIMENTAL DETAILS

#### A. Fabrication of AlGaN/GaN grating-gate PC structures

An AlGaN/GaN high electron mobility material system is chosen for the experimental studies. This type of heterostructure provides high electron density (up to  $10^{13}$  cm<sup>-2</sup>) on the AlGaN/GaN interface, which is difficult to achieve in any other 2D system. Thanks to that, plasma oscillations in 2D GaN-based structures of micrometer size can easily reach THz frequencies.

AlGaN/GaN heterostructures are grown by the metal-organic vapor phase epitaxy method on a 4-inch-diameter, 500- $\mu$ m-thick semi-insulating SiC substrate. The semiconductor stack consists of a 2.4 nm GaN cap, a 20.5 nm Al<sub>0.25</sub>Ga<sub>0.75</sub>N barrier, and a 255 nm GaN buffer grown directly on 62-nm-thick AlN nuclear layer on SiC substrate. Heterostructure parameters including the permittivity of each layer are listed in Table I. During the fabrication of the plasmonic structures [schematically illustrated in Fig. 4(a)], we pay special attention to the quality of a Schottky barrier contact (grating-gate coupler) and Ohmic (source and drain) contacts to the 2DEG channel.

The Ohmic source and drain contacts (marked as *S* source and *D* drain in Fig. 4) are formed by thermal evaporation of a Ti/Al/Ni/Au (150/1000/400/500 Å) metal stack and following rapid thermal annealing at 800 °C in a nitrogen atmosphere for 60 s. Such a procedure allows achieving the contact resistance of  $0.75 \pm 0.08$  Ohm  $\times$  mm, which is measured using the transmission line method on 30 test structures.

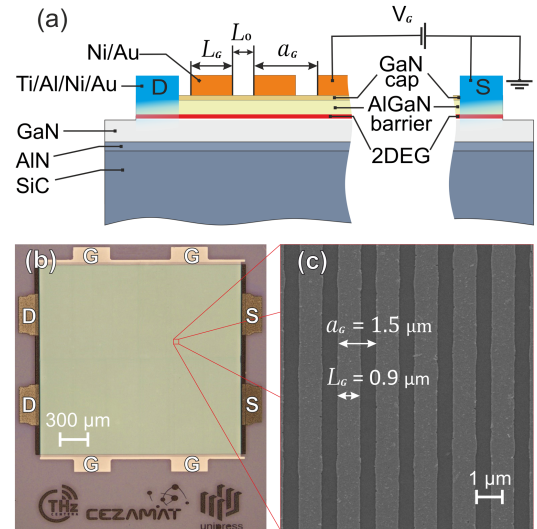


FIG. 4. Cross-section schematic view of the investigated PC structures (a), where *S* and *D* are source and drain terminals, respectively; optical microscope photo of one of the fabricated grating-gate PC structure (b); SEM image of a grating segment with  $a_g = 1.5$   $\mu$ m,  $L_g = 0.9$   $\mu$ m, and  $L_o = 0.6$   $\mu$ m (c).



In order to achieve the low leakage current in large-area grating-gate structures, a special procedure is used to fabricate the Schottky contacts. It starts with chemical cleaning of the AlGaIn surface. It includes the following steps: removing the possible organic contaminants by immersing the samples into an ultrasonic bath filled with dimethyl sulfoxide for 5 min followed by cleaning in acetone and isopropanol. Then, the natural surface oxides are removed by immersing the samples into 10% hydrofluoric acid for 5 min and 37% hydrochloric acid for 10 min. The chemical cleaning is finished by rinsing in deionized water and drying with an  $N_2$  gun.

To avoid any oxidation, after cleaning the samples are immediately placed in the vacuum chamber of an electron beam lithography (EBL) system. EBL patterning is performed on large  $1.7 \times 1.7 \text{ mm}^2$  active areas defining the grating gates. The exposed and developed samples are precisely cleaned from any photoresist residue using oxygen plasma in an inductively coupled plasma-reactive ion etching system. Finally, the grating gates are formed by thermal evaporation of Ni/Au (150/350 Å) and metal lift-off. The described procedure allows us to reach the gate leakage current density as low as  $J_{GS} \approx 10^{-6} \text{ A/cm}^2$ , which is sufficient to effectively control the 2DEG density under the large area ( $> 1 \text{ mm}^2$ ) metal gratings.

Three samples with different geometry of the grating-gate coupler are fabricated and investigated. A schematic cross section of investigated plasmonic structures is shown in Fig. 4(a). Optical microscope and scanning electron microscope (SEM) images of one of the studied devices are shown in Figs. 4(b) and 4(c), respectively. As can be seen in Fig. 4(b), all grating metal fingers are connected together. All structure terminals are provided with special pads for the bonding wires marked in Fig. 4(b) as “G,” “S,” and “D.” The 2D electron concentration  $n_G$  under the grating-gate electrode is controlled by the gate voltage  $V_G$ , referenced to the source and drain electrodes connected together. The geometrical parameters of the grating-gate coupler of the three investigated samples labeled as S13, S7, and S8 are listed in Table II.

## B. Electrical transport characterization

Before the grating deposition, bare AlGaIn/GaN heterostructures are characterized by capacitance-voltage measurements at 10 kHz using a mercury probe in order to estimate the ungated 2DEG concentration. The extracted value of  $n_0$  is  $8.7 \pm 0.9 \times 10^{12} \text{ cm}^{-2}$  at room temperature.

The transfer current-voltage characteristic of one of the grating-gate samples at  $T = 10 \text{ K}$  is shown in Fig. 5. It is characterized by a relatively high on/off ratio and a small subthreshold current, which is an indication of the small gate leakage current. The threshold voltage is determined from the linear extrapolation of the current-voltage characteristic to zero current. For all investigated structures, this value is in the range of  $V_{th} = -2.9 \pm 0.3 \text{ V}$ . We find  $V_{th}$  is

TABLE II. Grating-gate coupler parameters of investigated PC structures.

Structure parameters	S13	S7	S8
Grating period $a_G$	1.0 $\mu\text{m}$	1.5 $\mu\text{m}$	2.5 $\mu\text{m}$
Gated region width $L_G$	0.5 $\mu\text{m}$	0.9 $\mu\text{m}$	1.8 $\mu\text{m}$
Ungated region width $L_O$	0.5 $\mu\text{m}$	0.6 $\mu\text{m}$	0.7 $\mu\text{m}$
Filling factor $f$	0.50	0.60	0.72
Active area	$1.7 \times 1.7 \text{ mm}^2$	$1.7 \times 1.7 \text{ mm}^2$	$1.7 \times 1.7 \text{ mm}^2$
Number of grating cells $N_{GC}$	1650	1100	660

only weakly dependent on temperature. Therefore, the carrier density is virtually temperature independent.

The 2DEG concentration under the gate,  $n_G$ , for the above threshold regime can be found from the transfer current-voltage characteristics using Eq. (17). This yields the value of  $6.2 \pm 0.6 \times 10^{12} \text{ cm}^{-2}$  at  $V_0 = 2.9 \text{ V}$ . The  $n_G(V_0)$  dependence is shown in Fig. 5 by the red line. The dc electron mobility of 2DEG in the fabricated samples is estimated as  $\mu = [g_{m0}L_G N_{GC}]/[CW(V_D - IR_{acc})]$ , where  $g_{m0}$  is the intrinsic transconductance calculated taking into account the access resistance  $R_{acc}$  consisting of contact resistances and the resistance of ungated regions,  $I$  is current,  $V_D$  is drain voltage,  $C$  is the gate capacitance per unit area,  $N_{GC}$  is a number of grating cells (see Table II), and  $W = 1.7 \text{ mm}$  is the total width of the sample. This method provides  $\mu = 7500 \text{ cm}^2/\text{V} \cdot \text{s}$  at 10 K.

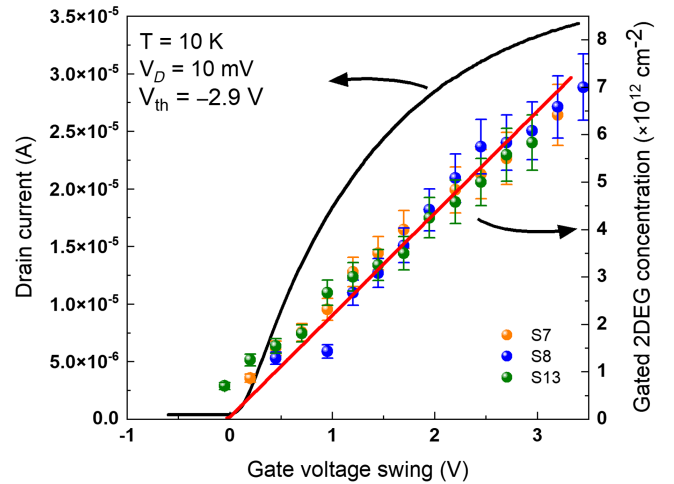


FIG. 5. Transfer current-voltage characteristic of the investigated PC structure measured at 10 K and drain-to-source voltage  $V_D = 10 \text{ mV}$ . The red line shows  $n_G$  concentration calculated using Eq. (17). Carrier densities  $n_G(V_0)$  obtained from the fitting procedure of THz measurements are shown as data points.

### C. THz measurements

THz transmission spectra measurements of the bare AlGaIn/GaN heterostructure as well as PC structures are performed by Fourier-transform infrared (FTIR) vacuum spectrometer (Vertex 80v from Bruker, Billerica, Massachusetts, USA) integrated with a continuous flow liquid helium cryostat. In order to reduce optical losses, the original cryostat windows are replaced by polymethylpentene (TPX) windows. The FTIR spectrometer is equipped with a mercury lamp source, a solid-state silicon beam splitter, a cryogenically cooled silicon bolometer, and a 3 THz low pass filter. The experimental spectral range is limited to 3 THz, because at higher frequencies the strong phonon absorption of the SiC substrate [64] interferes with the 2DEG plasmonic resonance spectra.

FTIR measurements are taken in a fast scanning mode at a mirror movement frequency of 5 kHz, with an interferogram average of 100 scans. Spectroscopy measurements are taken with a 1.5 mm aperture positioned close to the grating structure, allowing *em* radiation to transmit only through the grating-gate active region. A polypropylene film-based linear polarizer is also used in front of the sample. In Fig. 6, we show an example of the transmittance spectra measured at two different resolutions 1 and 4  $\text{cm}^{-1}$ . The spectra registered at the higher resolution show Fabry-Pérot (FP) fringes, which are caused by multiple internal reflections from the optically thick 500  $\mu\text{m}$  SiC substrate. In most of the experiments, we use the lower resolution, for which the FP interference is smeared out leaving well-visible plasmonic resonances. For more details, see Supplemental Material [62]: peculiarities of THz spectra fitting. All measurements are conducted at 10 K.

### IV. ELECTRICAL CONTROL OF PLASMONIC CRYSTAL SPECTRA

As pointed out in Sec. II, the resonant structure of the transmission spectra is strongly dependent on the modulation degree of 2DEG. The latter can be controlled by the

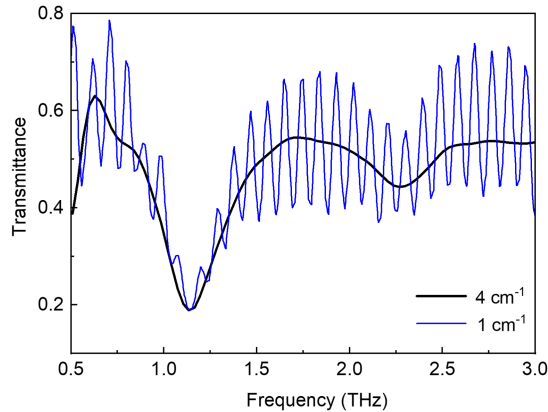


FIG. 6. Experimental transmittance of S7 PC sample at  $V_G = 0$  V ( $V_0 = 2.9$  V) measured at different spectral resolutions.

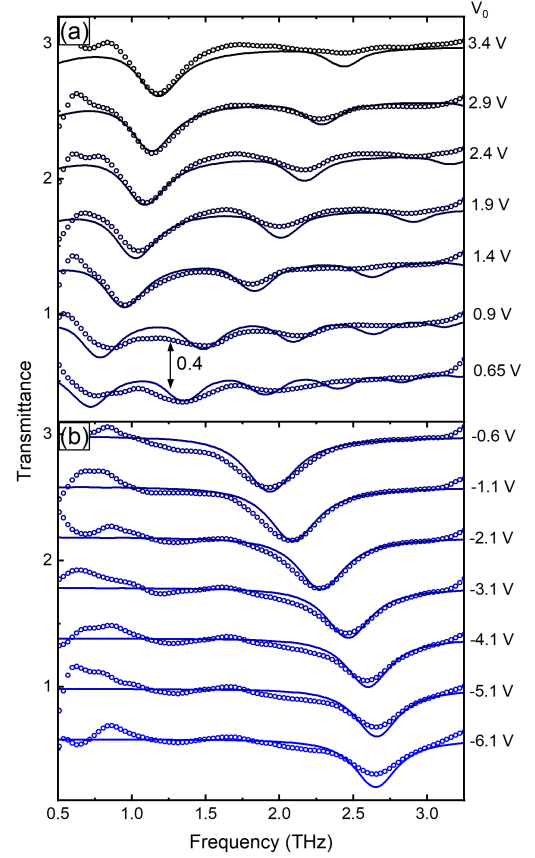


FIG. 7. Transmission spectra of the S7 PC sample at different gate-to-channel voltages:  $V_0 > 0$  (a) and  $V_0 < 0$  (b). Dotted and solid curves are the results of measurements and calculations, respectively.

gate voltage. Figure 7(a) shows experimental and calculated transmission spectra of the grating-gated S7 PC sample in the range of gate-to-channel voltages corresponding to modulation degree  $\rho < 1$ . This particular regime is referred to the delocalized phase of the PC.

As can be seen in Fig. 7(a), at  $V_0 = 3.4$  V two resonances at 1.18 and 2.83 THz exist within the experimental frequency band. With the decrease of the gate voltage swing, one can see the gradual redshift of these two main plasmon resonances ( $k = 1, 2$ ) and the emergence of higher-order resonances. As the gate voltage is approaching the threshold value, the resonance structure tends to vanish. Generally, with a decrease of the  $V_0$ , the number of resonances increases, but they become less intensive. At  $V_0 = 0.65$  V, the calculations predict the emergence of five resonances, but only the first three resonances can be seen in the experiment.

In the subthreshold regime  $V_0 < 0$ , the localized phase of the PC is realized with only one resonance in the considered frequency range [see Figs. 7(b) and 8(a)]. With a decrease of  $V_0$ , we observe a significant blueshift of discussed resonance from frequency 1.93 (at  $V_0 = -0.6$  V) to 2.64 THz (at  $V_0 = -6.1$  V). This is an unexpected

behavior, because at this range there are no carriers in the gated range and THz radiation is absorbed mainly in the ungated parts. As seen in Fig. 3(a), the simple theoretical model predicts in this case that plasma resonance frequency should be gate voltage independent. We interpret this behavior as due to the additional shrinking of the ungated region width  $L_O^{2D}$  as a result of the gate voltage applied between the gate and the ungated part of the channel. Such modification of the channel profile has been reported for the AlGaIn/GaN FET with side gates [72,73].

In the fitting procedure for subthreshold voltages, we vary  $\Delta x$  in order to account for the decrease of width  $L_O^{2D} = a_G - L_G - 2\Delta x$  at constant values of  $n_O$  and  $n_G = 0$ . Note, hereafter, all theoretical curves relating to transmission spectra are presented in terms of the quantity  $\langle T_\nu \rangle_{FP}$ , which is the transmission coefficient calculated for an optically thick substrate with following averaging over a period of FP fringes.

Figure 8 shows the experimental contour plots of the transmission spectrum  $T_\nu$  in the plane  $V_0 - \nu$  and the calculated one  $\langle T_\nu \rangle_{FP}$  for S7 PC sample. Dashed lines in Fig. 8(a) show the calculated frequency of the transmission minima.

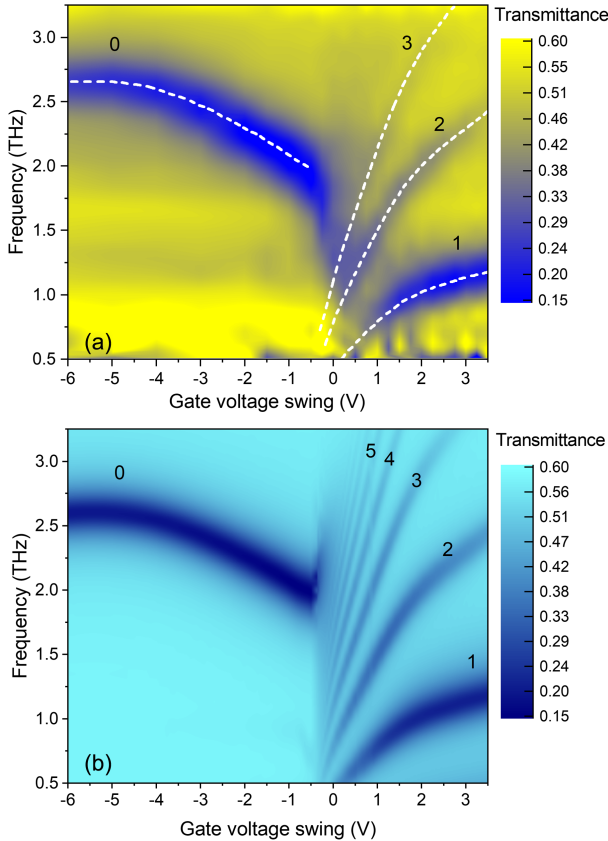


FIG. 8. Experimental (a) contour plot of the transmittance  $T_\nu$  and theoretical (b) contour plot of the transmittance  $\langle T_\nu \rangle_{FP}$  of the S7 sample. Dashed curves in (a) show the positions of the transmission minima extracted from the calculations.

The plots in Fig. 8 allow us to follow the dependencies of the plasmon resonances versus frequency and gate voltage. As seen in Fig. 8(b), calculations predict the existence of 4–5 resonances in the delocalized PC phase. Two of them can be clearly identified in the corresponding experimental contour plot shown in Fig. 8(a). In calculations, at  $V_0 \geq 0.9$  V, the lowest-frequency resonance is the most intensive and corresponds to the fundamental excitation of the 2D plasmon resonance with  $k = 1$ . The resonances enumerated as 2 and 3 are realized in the higher frequencies, but they are less intense.

As seen in Figs. 8(a) and 8(b), in the narrow region of the near-threshold voltages, the localized plasmon phase of 2DEG strip grating associated with ungated regions starts to form. At below threshold voltages, from  $V_0 = -0.5$  V to  $V_0 = -6$  V, an increase in the frequency of this resonance with saturation at higher gate voltages is observed. The general features of the experimental contour plot [Fig. 8(a)] are well traced by the calculation [Fig. 8(b)]. Particularly, the frequencies of the main resonances and their gate voltage dependencies are well reproduced by the simulations.

For completeness, we present the same experimental contour plots for S13 and S8 PC samples in Figs. 9(a) and 9(b). For these samples, the general resonant structure

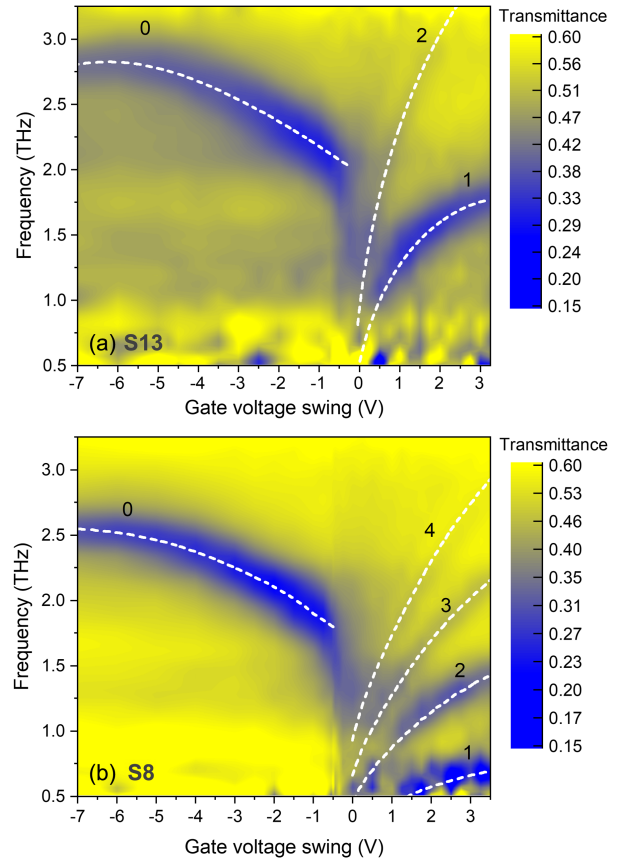


FIG. 9. Experimental contour plots of the transmittance  $T_\nu$  of the S13 (a) and S8 (b) samples. Dashed curves show the positions of the transmission minima extracted from the calculations.

of transmission spectra, their evolution versus gate voltage, and the transition between plasmon resonance regimes are also well reproduced by simulations (dashed lines show the calculated resonance frequencies).

However, the sharpness of both plasmon phases, delocalized and localized, become less pronounced for the S13 PC sample which has the smallest filling factor  $f = 0.5$ . It is a general property of the grating-gated PC structures for which the wider-slit metallic gratings provide the weaker coupling between *em* wave and plasmon oscillations of 2DEG. Moreover, due to the symmetry of the metallic grating of this sample ( $L_0 = L_G$ ), the plasmon modes in a uniform 2DEG channel with  $k = 2, 4, \dots$  are very weakly excited (this peculiarity is pointed out in Refs. [11,61]). Thus, in the experiment at  $V_0 > 0$ , we can clearly resolve only the fundamental mode of 2D plasmon resonance. In comparison with the S7 PC sample, due to the smaller grating period and the smaller grating filling factor, the resonant frequencies of S13 PC sample are shifted to the higher frequencies. For example, at  $V_0 = 2$  V the resonant frequency is equal to 1.57 THz (1.04 THz for the S7 sample at the same voltage swing). Because of the smaller width of the ungated region ( $0.5 \mu\text{m}$ ), the localized plasmon resonance is also at a slightly higher frequency.

For the S8 PC sample ( $a_G = 2.5 \mu\text{m}$ ,  $f = 0.72$ ), the resonant picture of the transmission spectra [see Fig. 9(b)] is very close to the S7 PC sample. At least, three first resonances are well resolved in the experiments and well reproduced by theoretical calculations. However, the larger grating period and larger filling factor of the S8 sample provide resonances at lower frequencies, compared to S7 and S13 samples. At  $V_0 < 1.5$  V, the resonant frequency of the fundamental resonance is out of our experimental spectral range. Because of the larger width of the ungated region ( $0.7 \mu\text{m}$ ), the localized plasmon resonance is also realized in the lower frequency range. Therefore, the resonance for gate voltage swing  $V_0 = -5$  V is observed at 2.45 THz. For all three samples, the gate voltage dependencies of the localized and delocalized plasmon frequencies are well reproduced by simulations.

In the fitting procedure, we use carrier density in the gated region  $n_G$  as the fitting parameter. The obtained values are shown in Fig. 5 together with the results of the electrical transport characterization. One can see that the values used in simulations are very close to those extracted from dc measurements.

Figure 10 illustrates the relationship between the gate voltage used in simulations and the resulting change in  $\Delta x$ . It is evident that the dependencies of  $\Delta x$  versus  $V_0$  exhibit similar behavior across all three samples. Although the width of the ungated region undergoes a certain level of alteration, the observed increase does not exceed 10% in any of the samples. Thus, the change in the width of the ungated region is relatively small.

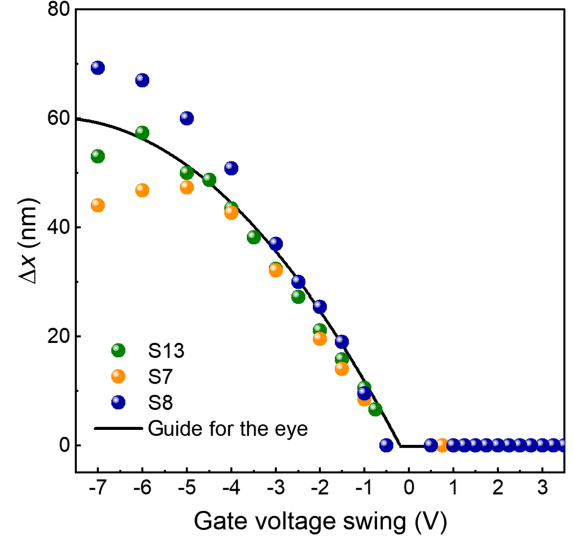


FIG. 10. The gate voltage dependencies of the additional depletion length  $\Delta x(V_0)$  (dots); the solid black line is shown as a guide for the eye.

## V. DISCUSSION AND ANALYSIS

### A. Delocalized phase of plasmonic crystal ( $V_0 > 0$ )

To better understand the importance of plasmonic crystal approximation, let us consider in more detail the experimental transmission spectra for the structure S7 at  $V_0 = 2.9$  V reproduced once again in Fig. 11. The solid line in this figure shows the result of rigorous electrodynamic simulation. As seen, the simulation reproduces the experimental data very well, including the position of the first- and second-order resonances. The best fit is obtained at electron concentrations  $n_0 = 8.0 \times 10^{12} \text{ cm}^{-2}$  and

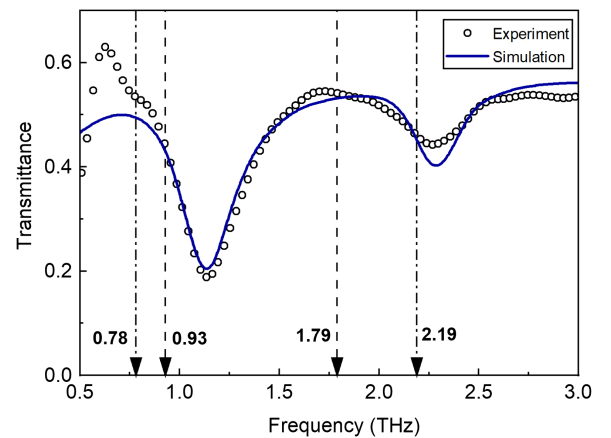


FIG. 11. Experimental  $T_\nu$  and simulated  $\langle T_\nu \rangle_{\text{FP}}$  transmittance of S7 PC sample at  $V_G = 0$  V ( $V_0 = 2.9$  V). Vertical arrows show the positions of the first- and second-order gated plasmon resonances calculated under the single-cavity assumption (dash-dotted lines) and assuming the wave vector defined by the grating period (dashed lines).

$n_G = 5.5 \times 10^{12} \text{ cm}^{-2}$  in the ungated and gated regions, respectively (modulation degree  $\rho = 0.19$ ). For dc mobility of 2DEG, we choose the value obtained from electrical characterization (see Sec. III B). The values of the parameters obtained from fitting (for more details, see Supplemental Material [62]) of the optical spectrum are in good agreement with the values obtained from electrical characterization (see Sec. III B).

In this section, we also aim to compare our model with other simpler approaches. One such method involves estimating the frequencies of the plasmon absorption lines through analytical means. Specifically, we can assume a single-cavity description of plasmons and estimate the resonant frequencies. Under this approximation, the grating-gate structure's unit cell breaks down into ungated and gated sections. These sections can work as cavities with symmetric boundaries for ungated and gated plasmons, separately. Their resonant frequencies can be estimated using Eq. (1) (with corresponding effective permittivities) taking

$$q_k = (2k - 1)\pi/L_O \quad \text{and} \quad n = n_O \quad (18)$$

for the ungated plasmons localized under the grating openings and

$$q_k = (2k - 1)\pi/L_G \quad \text{and} \quad n = n_G \quad (19)$$

for the gated plasmons localized under the grating strips.

The frequencies of the first and second harmonics for the gated plasmons are shown in Fig. 11 by dash-dotted lines. As can be seen, this estimate is very far from the experimental situation. In some publications, the plasmon frequencies are calculated assuming the wave vector defined by the grating period  $q_k = 2\pi k/a_G$ . The first- and second-order frequencies for the gated plasmons obtained in this approach are shown as the vertical dashed lines in Fig. 11. One can see that the simple analytical approaches produce results far from the experimental ones and in any case cannot be used to describe the grating-gate structure, which should be considered as a PC with strong interaction of the gated and ungated parts.

Additionally, the shape of a spectral line of the first-order plasmon resonance can be well approximated by the Lorentz-type function [11,51]. Using the following approximation of transmission spectra:

$$T_\nu^{(a)} = \frac{T_{\max}(\nu^2 - \nu_{r,1}^2)^2 + T_{\min}\Delta^2\nu^2}{(\nu^2 - \nu_{r,1}^2)^2 + \Delta^2\nu^2}, \quad (20)$$

where  $T_{\max} = 0.5$ ,  $T_{\min} = 0.2$ , resonant frequency  $\nu_{r,1} = 1.13 \text{ THz}$ , and full width at half maximum (FWHM),  $\Delta = 0.25 \text{ THz}$ , the obtained quality factor  $\text{QF} = \nu_{r,1}/\Delta$  is equal to 4.52. It should be noted that a linewidth of 2D plasmon resonances in PC structures is determined by the

sum of two contributions  $\gamma_e$  and  $\Gamma_e$  being the nonradiative and the radiative decay rates [74], respectively, i.e.,  $\Delta = [\gamma_e + \Gamma_e]/2\pi$ . The nonradiative decay rate associates with electron scattering,  $\gamma_e = 1/\tau$ . The radiative decay rate describes the radiative losses of 2D electrons due to reemission of the electromagnetic waves. The  $\Gamma_e$  depends on geometry of the grating and dielectric surrounding of the 2DEG as well as on the order of plasmon resonance. In the general case, there is no simple analytic formula for  $\Gamma_e$ . However, we can estimate  $\Gamma_e$  as follows:  $\Gamma_e = 2\pi\Delta - \gamma_e$ . For  $\gamma_e = 1.17 \text{ THz}$  ( $\tau = 0.85 \text{ ps}$ ),  $\Gamma_e = 0.4 \text{ THz}$ . One can see that the electron momentum scattering is the main mechanism determining the linewidth and quality factor of the discussed plasmon resonance.

Also, we calculate the relative error  $\delta T$  between theoretical  $\langle T_\nu \rangle_{\text{FP}}$  and experimental  $T_\nu$  curves as follows:  $\delta T = \int_{\nu_1}^{\nu_2} |\langle T_\nu \rangle_{\text{FP}} - T_\nu| d\nu / \int_{\nu_1}^{\nu_2} T_\nu d\nu$ . We obtain that, in the spectral range of 0.5–3 THz,  $\delta T = 5\%$  for curves depicted in Fig. 11. We suggest that a small discrepancy between theoretical and experimental results can be associated with several factors: (i) features of optical measurements (effect of conical form of the THz beam, deviation from normal incidence and TM polarization, additional optical losses in the optical alignment), (ii) fluctuations of the grating period, (iii) possible influence of the frequency dispersion of optically thick SiC substrate, and (iv) model of the steplike concentration profile of 2DEG.

To get a better understanding of the physical situation, we perform the numerical calculations of the electric field profile and absorptivity. Figure 12 shows the calculated near-field patterns for the first [Fig. 12(a)] and second [Fig. 12(c)] harmonics for the S7 structure at  $V_G = 0 \text{ V}$  ( $V_0 = 2.9 \text{ V}$ ). Particularly, we pay attention to the spatial distributions of the  $x$  component of the electric field  $E_x(x, z)$  of the  $em$  wave in the vicinity of the metallic grating and 2DEG. This component can be used for the calculation of local absorptivity of 2DEG,  $A^{2D}$  [61]:

$$A^{2D}(x) = \frac{4\pi\text{Re}[\sigma^{2D}(x)]}{c} \times \frac{|E_x(x, z_1)|^2}{\int_0^{a_G} |E_0|^2 dx}, \quad (21)$$

where  $\text{Re}[\sigma^{2D}(x)]$  is the real part of the conductivity profile of 2DEG and  $z_1$  is the  $z$  coordinate of 2DEG.

As seen in Figs. 12(a) and 12(c), the  $em$  field in the near-field zone of the considered plasmonic structure has a strongly nonuniform distribution. The field concentration effect is clearly seen near the ridges of the metallic fingers. Also, it is observed the essential increase of the amplitude,  $|E_x|$ , in the gated region of 2DEG (4 times larger than the amplitude of the incident wave,  $E_0$ ). The latter is associated with the excitation of the fundamental [Fig. 12(a)] and second-order [Fig. 12(c)] plasmon resonances. The spatial distribution of both amplitude  $|E_x(x)(x, z)|$  and local absorptivity  $A^{2D}(x)$  [see Figs. 12(b) and 12(d)] acquire oscillatinglike behavior in the gated region with almost flat

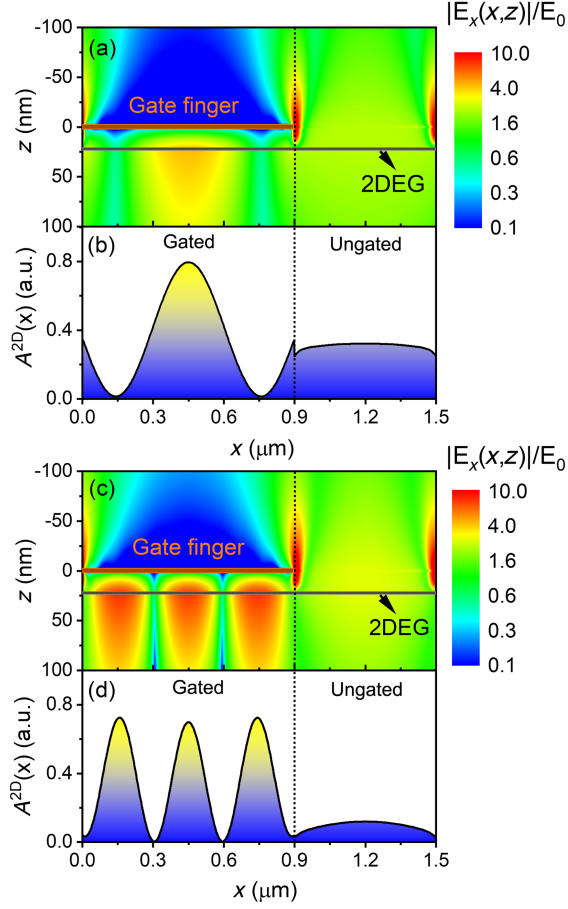


FIG. 12. Spatial distributions of the amplitude of  $E_x$  component of  $em$  field (a),(c) and local absorptivity (b),(d) in one period of PC at  $V_G = 0$  V ( $V_0 = 2.9$  V). Results in (a) and (b) are calculated for fundamental plasmon resonance at 1.2 THz. (c) and (d) correspond to the second-order resonance at 2.4 THz [see black stars in the contour plot in Fig. 3(a)].

distribution in the ungated region of 2DEG. The discontinuity of quantity  $A^{2D}(x)$  at  $x = L_G$  is the result of the assumed model of the abrupt steplike concentration profile of 2DEG.

Since these calculations show that the  $em$  energy absorbs both, in the gated and ungated regions, we can indeed call this regime delocalized plasmonic crystal.

### B. Localized phase of plasmonic crystal ( $V_0 < 0$ )

Figure 13 shows the results of near-field calculations for the localized phase of PC. In contrast to the delocalized plasmon crystal situation (previous section), the energy concentration effect becomes larger. At this, the energy of the  $em$  wave is mainly concentrated in the region of the metallic grating opening. Particularly, the hot zone (high electric field) occurs near the edges of metallic fingers and strips of the formed 2DEG grating. Note that the  $em$  wave practically does not penetrate under the metallic gate where the cold zone is formed. The spatial distributions of the  $x$

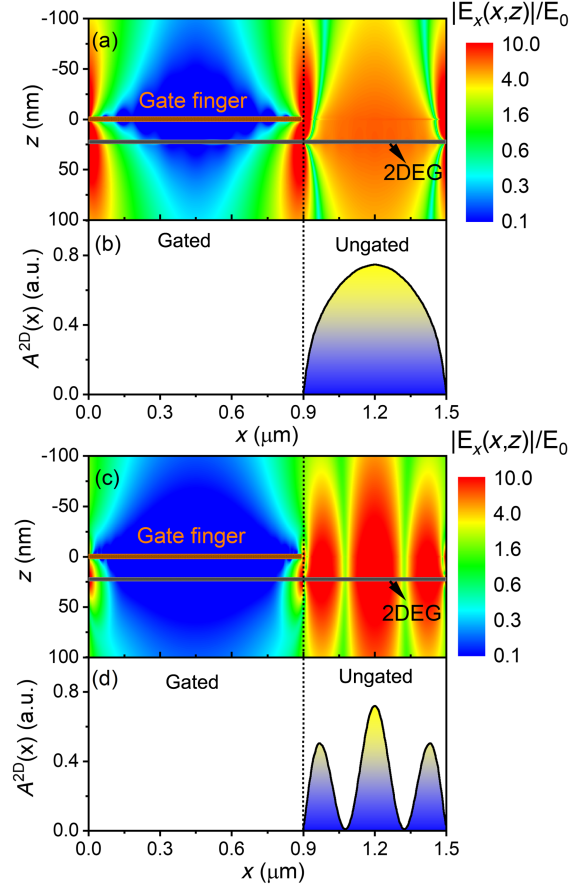


FIG. 13. Spatial distributions of the amplitude of  $E_x$  component of  $em$  field (a),(c) and local absorptivity (b),(d) in one period of PC at  $V_G = -3$  V ( $V_0 = -0.1$  V). Results in (a) and (b) are calculated for the fundamental plasmon resonance at 2.3 THz. (c) and (d) correspond to the second-order resonance at 6.1 THz [see red stars in the contour plot in Fig. 3(a)].

component of  $em$  wave in the plane of 2DEG and the local absorptivity [see Figs. 13(b) and 13(d)] show that in this regime an ungated part of 2DEG works as a resonant cavity. Particularly, for fundamental resonance (2.3 THz), the plasmon oscillation has a half-wavelength localization on the width of the grating opening. For the second-order resonance (6.12 THz), the three half-wavelength localization is clearly seen. As seen in Fig. 13, the  $em$  energy absorbs only within gate openings. Thus, we call this regime the localized phase of PC.

The introduced terms delocalized and localized phases emphasize the main physical difference between plasmon resonances observed above and below threshold voltages. The near-field calculations (Figs. 12 and 13) emphasize the main physical differences between these two phases. As seen from the patterns of the spatial distribution of the local absorptivity [compare Figs. 12(b) and 13(b) for the first harmonic and compare Figs. 12(d) and 13(d) for the second one] in the delocalized phase the absorption of THz radiation extends over the whole period (ungated

and gated regions) of the structure; i.e., 2D plasmons are excited in a whole of 2DEG grating-gate structure. In the localized scenario, the region of 2DEG under the gate is totally depleted, and the THz radiation absorption is localized only in the ungated regions. The “new” plasmonic structure—grating of the 2DEG-ungated strips separated by metallic grating fingers—is formed. In this new plasmonic structure, THz radiation excites only plasmons localized in the electrically formed ungated 2DEG-strip grating. Only these localized ungated parts of 2DEG effectively absorb THz radiation. However, the whole structure responds to incoming radiation as a PC, because the localized plasmons interact through the metal grating. As shown below, ignoring the metal grating modifies the resonance spectra significantly.

The experimental transmission spectra for the structure S7 at  $V_0 = -0.6$  V are reproduced once again in Fig. 14. As seen, the experiment and simulations are in good agreement. At this, the FWHM,  $\Delta = 0.55$  THz, the quality factor  $QF = 3.5$  at resonant frequency of 1.93 THz and estimation of radiative decay rate gives that  $\Gamma_e = 1.96$  THz. The relative error  $\delta T$  is equal to 8.5%.

We can again attempt to estimate the frequency of the plasmon absorption line analytically using the simple approach. The frequency of the ungated plasmon fundamental resonance can be estimated using Eq. (18) giving  $\nu_{r,1} = 3.9$  THz, which is far beyond the experimental and simulated values. In order to understand the role of the metal grating, we perform the simulation of the structure neglecting metallic gates, i.e., the structure consisting only of the ungated parts separated by a region with zero electron concentration. The result is shown in Fig. 14 by the violet line. As seen, this approach does not give the correct description of the experimental situation.

Considering different simplified approaches, we conclude that, even in the absence of carriers under the gated regions, the plasma oscillations of the system cannot be

simplified as a sum of independent plasmonic oscillators in the ungated sections. Therefore, the plasmon resonances can be accurately described only using the full PC approximation.

## VI. CONCLUSIONS

We have experimentally and theoretically investigated resonant properties of large area ( $1.7 \times 1.7$  mm<sup>2</sup>) grating-gate AlGaIn/GaN plasmonic crystal structures in the THz frequency range. Advanced nanometer grating-gate technology allowed us to investigate THz plasma excitations in a wide range of gate voltages, thereby exploring various regimes of carrier density modulation.

The results of THz measurements were analyzed by rigorous electrodynamic simulations including contour plots of the  $em$  field in the near-field zone of the PC structure. The computational algorithm was based on the numerical solution of Maxwell’s equations within the method of the integral equations. The developed method exhibited a high efficiency with respect to convergence and computational time.

We found that the experimental and calculated resonant structure of the transmission spectra including its modification versus gate voltage corresponds to the formation of two different phases of PC structure depending on the 2DEG carrier density modulation profile.

Particularly, at above-threshold voltages  $V_0 > 0$  and small modulation degree  $\rho \leq 0.2$ , the well-developed delocalized phase of PC is realized. This phase is associated with several resonances in transmission spectra corresponding to different orders of 2D plasmon excitations under the grating. The spatial distribution of the electric field associated with these plasmon excitations (as well as the local absorptivity of THz radiation) extends over the whole period of the structure; i.e., 2D plasma is simultaneously excited in both ungated and gated regions of 2DEG.

With further gate voltage decrease and approaching the threshold voltage, the transition between delocalized and localized phases of PC starts to form. At this, the multi-resonant structure in transmission spectra disappears, higher-order harmonics with frequencies resonant with localized plasmons are amplified, and, finally, they transform into a new strong localized phase. In contrast to the delocalized phase, the localized phase has spatial localization of the electric field (as well as the local absorptivity of THz radiation) in the ungated part of 2DEG. However, the metal grating still plays an important role, and the whole structure behaves like a PC. Even if almost the whole  $em$  energy is absorbed in the ungated parts, the experimental results cannot be explained using only single-cavity approaches. This is due to the fact that one always has to consider the presence of the metallic grating that partially screens the plasmon oscillations in the 2DEG strips and enhances the coupling of this plasmon resonance with incident radiation.

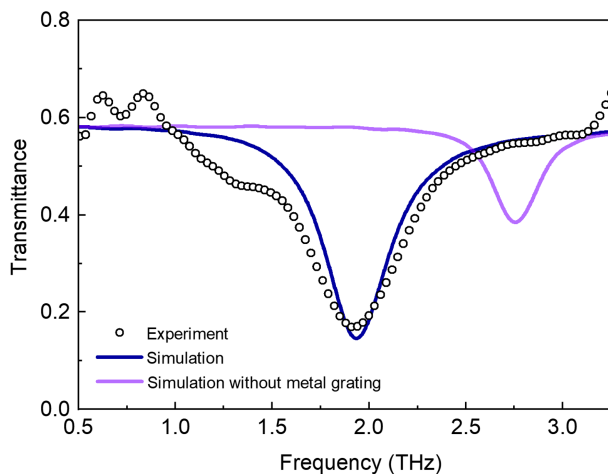


FIG. 14. Experimental  $T_\nu$  and simulated  $\langle T_\nu \rangle_{FP}$  transmittance of the S7 PC sample at  $V_G = -3.5$  V ( $V_0 = -0.6$  V).

The general picture of the transformation of PC states from delocalized to localized phases was traced in THz experiments for all three samples with different geometry of the grating coupler. Moreover, we observed that a decrease of  $V_G$  below the threshold ( $\rho \sim 1$ ) leads to an essential blueshift of the resonance in the localized phase of the PC structure. This phenomenon was explained by the reduction of the ungated part's effective width by negative gate voltage below the threshold (side or edge gate effect).

Our research presents the first experimental evidence of electrically tunable transitions between different phases of THz PCs. The remarkable congruence between our experimental data and calculated values supports the theoretical approach and affirms the physical understanding of all observed phenomena. While our experiments focused on grating-gate structures based on AlGaIn/GaN heterojunctions, the findings hold general relevance and can be extended to other semiconductor-based PC structures. Therefore, our experimental and theoretical results are crucial steps toward a deeper understanding of THz plasma physics and the development of all-electrically tunable devices for THz optoelectronics.

#### ACKNOWLEDGMENTS

This work was supported by the “International Research Agendas” program of the Foundation for Polish Science is cofinanced by the European Union under the European Regional Development Fund for CENTERA Lab (No. MAB/2018/9) and cofunded by the European Union (ERC “TERAPLASM,” Project No. 101053716). Views and opinions expressed are, however, those of the author(s) only and do not necessarily reflect those of the European Union or the European Research Council. Neither the European Union nor the granting authority can be held responsible for them. P. S. and M. S. are grateful for the partial support was provided by the National Science Centre, Poland allocated on the basis of Grants No. 2019/35/N/ST7/00203 and No. 2020/38/E/ST7/00476. V. V. K., Y. M. L., and S. M. K. acknowledge the long-term program of support of the Ukrainian research teams at the Polish Academy of Sciences carried out in collaboration with the U.S. National Academy of Sciences with the financial support of external partners. S. M. K. is grateful to Technical University of Dortmund, where Comsol calculations were performed. Also, the work was partially supported by Science and Technology Center in Ukraine (STCU) in collaboration with the Institute of Magnetism of NAS of Ukraine and MES of Ukraine (Project No. 9918). The authors express their gratitude to Professor V. A. Kochelap (ISP NASU) and Professor A. E. Belyaev (ISP NASU) for their valuable interest in this work.

- [1] T. Otsuji and M. Shur, *Terahertz Plasmonics: Good Results and Great Expectations*, *IEEE Microw. Mag.* **15**, 43 (2014).
- [2] M. S. Shur, *Terahertz Plasmonic Technology*, *IEEE Sens. J.* **21**, 12752 (2021).
- [3] S. Huang, C. Song, G. Zhang, and H. Yan, *Graphene Plasmonics: Physics and Potential Applications*, *Nanophotonics* **6**, 1191 (2017).
- [4] W. Knap, M. Dyakonov, D. Coquillat, F. Teppe, N. Dyakonova, J. Łusakowski, K. Karpierz, M. Sakowicz, G. Valusis, D. Seliuta *et al.*, *Field Effect Transistors for Terahertz Detection: Physics and First Imaging Applications*, *J. Infrared Millimeter Terahertz Waves* **30**, 1319 (2009).
- [5] E. Shaner, M. Lee, M. Wanke, A. Grine, J. Reno, and S. Allen, *Single-Quantum-Well Grating-Gated Terahertz Plasmon Detectors*, *Appl. Phys. Lett.* **87**, 193507 (2005).
- [6] V. Popov, D. Fateev, T. Otsuji, Y. Meziani, D. Coquillat, and W. Knap, *Plasmonic Terahertz Detection by a Double-Grating-Gate Field-Effect Transistor Structure with an Asymmetric Unit Cell*, *Appl. Phys. Lett.* **99**, 243504 (2011).
- [7] Y. Kurita, G. Ducournau, D. Coquillat, A. Satou, K. Kobayashi, S. Boubanga Tombet, Y. Meziani, V. Popov, W. Knap, and T. Suemitsu, *Ultrahigh Sensitive Sub-terahertz Detection by InP-Based Asymmetric Dual-Grating-Gate High-Electron-Mobility Transistors and Their Broadband Characteristics*, *Appl. Phys. Lett.* **104**, 251114 (2014).
- [8] H. Spisser, A.-S. Grimault-Jacquín, N. Zerounian, A. Aassime, L. Cao, F. Boone, H. Maher, Y. Cordier, and F. Aniel, *Room-Temperature AlGaIn/GaN Terahertz Plasmonic Detectors with a Zero-Bias Grating*, *J. Infrared Millimeter Terahertz Waves* **37**, 243 (2016).
- [9] J. Delgado-Notario, W. Knap, V. Clerico, J. Salvador-Sanchez, J. Calvo-Gallego, T. Taniguchi, K. Watanabe, T. Otsuji, V. V. Popov, and D. Fateev, *Enhanced Terahertz Detection of Multigate Graphene Nanostructures*, *Nanophotonics* **11**, 519 (2022).
- [10] M. Dyakonov and M. Shur, *Shallow Water Analogy for a Ballistic Field Effect Transistor: New Mechanism of Plasma Wave Generation by dc Current*, *Phys. Rev. Lett.* **71**, 2465 (1993).
- [11] S. A. Mikhailov, *Plasma Instability and Amplification of Electromagnetic Waves in Low-Dimensional Electron Systems*, *Phys. Rev. B* **58**, 1517 (1998).
- [12] V. Kachorovskii and M. Shur, *Current-Induced Terahertz Oscillations in Plasmonic Crystal*, *Appl. Phys. Lett.* **100**, 232108 (2012).
- [13] S. A. Mikhailov, N. A. Savostianova, and A. S. Moskalenko, *Negative Dynamic Conductivity of a Current-Driven Array of Graphene Nanoribbons*, *Phys. Rev. B* **94**, 035439 (2016).
- [14] A. S. Petrov, D. Svintsov, V. Ryzhii, and M. S. Shur, *Amplified-Reflection Plasmon Instabilities in Grating-Gate Plasmonic Crystals*, *Phys. Rev. B* **95**, 045405 (2017).
- [15] D. Svintsov, *Emission of Plasmons by Drifting Dirac Electrons: A Hallmark of Hydrodynamic Transport*, *Phys. Rev. B* **100**, 195428 (2019).
- [16] V. V. Korotyeyev and V. A. Kochelap, *Plasma Wave Oscillations in a Nonequilibrium Two-Dimensional Electron Gas. Electric Field Induced Plasmon Instability in the Terahertz Frequency Range*, *Phys. Rev. B* **101**, 235420 (2020).



- [17] P. Cosme and H. Terças, *Terahertz Laser Combs in Graphene Field-Effect Transistors*, *ACS Photonics* **7**, 1375 (2020).
- [18] P. Cosme and H. Terças, *Hydrodynamical Study of Terahertz Emission in Magnetized Graphene Field-Effect Transistors*, *Appl. Phys. Lett.* **118**, 131109 (2021).
- [19] D. Zhang, Z. Xu, G. Cheng, Z. Liu, A. R. Gutierrez, W. Zang, T. Norris, and Z. Zhong, *Strongly Enhanced THz Generation Enabled by a Graphene Hot-Carrier Fast Lane*, *Nat. Commun.* **13**, 6404 (2022).
- [20] A. V. Chaplik, *Possible Crystallization of Charge Carriers in Low-Density Inversion Layers*, *Sov. J. Exp. Theor. Phys.* **35**, 395 (1972).
- [21] A. V. Chaplik, *Absorption and Emission of Electromagnetic Waves by Two-Dimensional Plasmons*, *Surf. Sci. Rep.* **5**, 289 (1985).
- [22] S. J. Allen, D. C. Tsui, and R. A. Logan, *Observation of the Two-Dimensional Plasmon in Silicon Inversion Layers*, *Phys. Rev. Lett.* **38**, 980 (1977).
- [23] D. Tsui, S. J. Allen, R. Logan, A. Kamgar, and S. Coppersmith, *High Frequency Conductivity in Silicon Inversion Layers: Drude Relaxation, 2D Plasmons and Minigaps in a Surface Superlattice*, *Surf. Sci.* **73**, 419 (1978).
- [24] D. Tsui, E. Gornik, and R. Logan, *Far Infrared Emission from Plasma Oscillations of Si Inversion Layers*, *Solid State Commun.* **35**, 875 (1980).
- [25] N. Nader Esfahani, R. Peale, W. Buchwald, C. Fredricksen, J. Hendrickson, and J. Cleary, *Millimeter-Wave Photoresponse due to Excitation of Two-Dimensional Plasmons in InGaAs/InP High-Electron-Mobility Transistors*, *J. Appl. Phys.* **114**, 033105 (2013).
- [26] M. Bialek, M. Czapkiewicz, J. Wróbel, V. Umansky, and J. Lusakowski, *Plasmon Dispersions in High Electron Mobility Terahertz Detectors*, *Appl. Phys. Lett.* **104**, 263514 (2014).
- [27] A. Muravjov, D. Veksler, V. Popov, O. Polischuk, N. Pala, X. Hu, R. Gaska, H. Saxena, R. Peale, and M. Shur, *Temperature Dependence of Plasmonic Terahertz Absorption in Grating-Gate Gallium-Nitride Transistor Structures*, *Appl. Phys. Lett.* **96**, 042105 (2010).
- [28] H. Qin, Y. Yu, X. Li, J. Sun, and Y. Huang, *Excitation of Terahertz Plasmon in Two-Dimensional Electron Gas*, *Terahertz Sci. Technol.* **9**, 71 (2016).
- [29] V. Jakštas, I. Grigelionis, V. Janonis, G. Valušis, I. Kašalynas, G. Seniutinas, S. Juodkazis, P. Prystawko, and M. Leszczyński, *Electrically Driven Terahertz Radiation of 2DEG Plasmons in AlGaN/GaN Structures at 110 K Temperature*, *Appl. Phys. Lett.* **110**, 202101 (2017).
- [30] V. Shalygin, M. Moldavskaya, M. Y. Vinnichenko, K. Maremyanin, A. Artemyev, V. Y. Panevin, L. Vorobjev, D. Firsov, V. Korotyeyev, A. Sakharov *et al.*, *Selective Terahertz Emission due to Electrically Excited 2D Plasmons in AlGaN/GaN Heterostructure*, *J. Appl. Phys.* **126**, 183104 (2019).
- [31] D. Pashnev, V. Korotyeyev, J. Jorudas, T. Kaplas, V. Janonis, A. Urbanowicz, and I. Kašalynas, *Experimental Evidence of Temperature Dependent Effective Mass in AlGaN/GaN Heterostructures Observed via THz Spectroscopy of 2D Plasmons*, *Appl. Phys. Lett.* **117**, 162101 (2020).
- [32] H. Yan, X. Li, B. Chandra, G. Tulevski, Y. Wu, M. Freitag, W. Zhu, P. Avouris, and F. Xia, *Tunable Infrared Plasmonic Devices Using Graphene/Insulator Stacks*, *Nat. Nanotechnol.* **7**, 330 (2012).
- [33] B. Yan, J. Fang, S. Qin, Y. Liu, Y. Zhou, R. Li, and X.-A. Zhang, *Experimental Study of Plasmon in a Grating Coupled Graphene Device with a Resonant Cavity*, *Appl. Phys. Lett.* **107**, 191905 (2015).
- [34] Z. Fei, A. S. Rodin, G. O. Andreev, W. Bao, A. S. McLeod, M. Wagner, L. M. Zhang, Z. Zhao, M. Thiemens, G. Dominguez, M. M. Fogler, A. H. Castro Neto, C. N. Lau, F. Keilmann, and D. N. Basov, *Gate-Tuning of Graphene Plasmons Revealed by Infrared Nano-imaging*, *Nature (London)* **487**, 82 (2012).
- [35] G. Ni, A. McLeod, Z. Sun, L. Wang, L. Xiong, K. W. Post, S. Sunku, B.-Y. Jiang, J. Hone, C. R. Dean, M. M. Fogler, and D. N. Basov, *Fundamental Limits to Graphene Plasmonics*, *Nature (London)* **557**, 530 (2018).
- [36] J. Chen, M. Badioli, P. Alonso-González, S. Thongrattanasiri, F. Huth, J. Osmond, M. Spasenović, A. Centeno, A. Pesquera, P. Godignon *et al.*, *Optical Nano-imaging of Gate-Tunable Graphene Plasmons*, *Nature (London)* **487**, 77 (2012).
- [37] P. Alonso-González, A. Y. Nikitin, Y. Gao, A. Woessner, M. B. Lundeberg, A. Principi, N. Forcellini, W. Yan, S. Vélez, A. J. Huber *et al.*, *Acoustic Terahertz Graphene Plasmons Revealed by Photocurrent Nanoscopy*, *Nat. Nanotechnol.* **12**, 31 (2017).
- [38] P. Cosme, J. S. Santos, J. Bizarro, and I. Figueiredo, *Tethys: A Simulation Tool for Graphene Hydrodynamic Models*, *Comput. Phys. Commun.* **282**, 108550 (2023).
- [39] O. Matov, O. Polischuk, and V. Popov, *Electromagnetic Emission from Two-Dimensional Plasmons in a Semiconductor-Dielectric Structure with Metal Grating: Rigorous Theory*, *Int. J. Infrared Millimeter Waves* **14**, 1455 (1993).
- [40] D. Fateev, V. Popov, and M. Shur, *Transformation of the Plasmon Spectrum in a Grating-Gate Transistor Structure with Spatially Modulated Two-Dimensional Electron Channel*, *Semiconductors* **44**, 1406 (2010).
- [41] V. V. Popov, *Plasmon Excitation and Plasmonic Detection of Terahertz Radiation in the Grating-Gate Field-Effect-Transistor Structures*, *J. Infrared Millimeter Terahertz Waves* **32**, 1178 (2011).
- [42] O. R. Matov, O. V. Polischuk, and V. V. Popov, *The Plasma Oscillations Spectrum of a Periodically Inhomogeneous 2D Electron System near the Perforation Threshold*, *J. Exp. Theor. Phys.* **95**, 505 (2002).
- [43] T. Watanabe, T. Fukushima, Y. Yabe, S. A. B. Tombet, A. Satou, A. A. Dubinov, V. Y. Aleshkin, V. Mitin, V. Ryzhii, and T. Otsuji, *The Gain Enhancement Effect of Surface Plasmon Polaritons on Terahertz Stimulated Emission in Optically Pumped Monolayer Graphene*, *New J. Phys.* **15**, 075003 (2013).
- [44] Y. Takatsuka, K. Takahagi, E. Sano, V. Ryzhii, and T. Otsuji, *Gain Enhancement in Graphene Terahertz Amplifiers with Resonant Structures*, *J. Appl. Phys.* **112**, 033103 (2012).
- [45] S. Boubanga-Tombet, S. Chan, T. Watanabe, A. Satou, V. Ryzhii, and T. Otsuji, *Ultrafast Carrier Dynamics and Terahertz Emission in Optically Pumped Graphene at Room Temperature*, *Phys. Rev. B* **85**, 035443 (2012).

- [46] C. Wimer, C. Kiener, W. Boxleitner, M. Witzany, E. Gornik, P. Vogl, G. Böhm, and G. Weimann, *Direct Observation of the Hot Electron Distribution Function in GaAs/AlGaAs Heterostructures*, *Phys. Rev. Lett.* **70**, 2609 (1993).
- [47] K. Tantiwanichapan, X. Wang, A. K. Swan, and R. Paiella, *Graphene on Nanoscale Gratings for the Generation of Terahertz Smith-Purcell Radiation*, *Appl. Phys. Lett.* **105**, 241102 (2014).
- [48] Y. Li, P. Ferreyra, A. Swan, and R. Paiella, *Current-Driven Terahertz Light Emission from Graphene Plasmonic Oscillations*, *ACS Photonics* **6**, 2562 (2019).
- [49] S. Lu, A. Nussupbekov, X. Xiong, W. J. Ding, C. E. Png, Z.-E. Ooi, J. H. Teng, L. J. Wong, Y. Chong, and L. Wu, *Smith-Purcell Radiation from Highly Mobile Carriers in 2D Quantum Materials*, *Laser Photonics Rev.* **17**, 2300002 (2023).
- [50] D. Pashnev, T. Kaplas, V. Korotyeyev, V. Janonis, A. Urbanowicz, J. Jorudas, and I. Kašalynas, *Terahertz Time-Domain Spectroscopy of Two-Dimensional Plasmons in AlGaIn/GaN Heterostructures*, *Appl. Phys. Lett.* **117**, 051105 (2020).
- [51] Y. Lyaschuk, V. Korotyeyev, and V. Kochelap, *Peculiarities of Amplitude and Phase Spectra of Semiconductor Structures in THz Frequency Range*, *Semi. Phys. Quant. Electron. Optoelectron.* **25**, 121 (2022).
- [52] S. Boubanga-Tombet, W. Knap, D. Yadav, A. Satou, D. B. But, V. V. Popov, I. V. Gorbenko, V. Kachorovskii, and T. Otsuji, *Room-Temperature Amplification of Terahertz Radiation by Grating-Gate Graphene Structures*, *Phys. Rev. X* **10**, 031004 (2020).
- [53] S. Rudin, *Temperature Dependence of the Nonlinear Plasma Resonance in Gated Two-Dimensional Semiconductor Conduction Channels*, *Appl. Phys. Lett.* **96**, 252101 (2010).
- [54] H. Totsuji, *Theory of Two-Dimensional Classical Electron Plasma*, *J. Phys. Soc. Jpn.* **40**, 857 (1976).
- [55] H. T. M. C. M. Baltar, K. Drozdowicz-Tomsia, and E. M. Goldys, *Propagating Surface Plasmons and Dispersion Relations for Nanoscale Multilayer Metallic-Dielectric Films*, in *Plasmonics*, edited by K. Y. Kim (IntechOpen, Rijeka, 2012), Chap. 6.
- [56] A. Huber, B. Deutsch, L. Novotny, and R. Hillenbrand, *Focusing of Surface Phonon Polaritons*, *Appl. Phys. Lett.* **92**, 203104 (2008).
- [57] Y. M. Lyaschuk and V. V. Korotyeyev, *Interaction of Terahertz Electromagnetic Field with a Metallic Grating: Near-Field Zone*, *Ukr. J. Phys. Opt.* **13**, 142 (2012).
- [58] Y. M. Lyaschuk and V. V. Korotyeyev, *Interaction of a Terahertz Electromagnetic Wave with the Plasmonic System “Grating-2D-Gas”. Analysis of Features of the Near Field*, *Ukr. J. Phys.* **59**, 495 (2014).
- [59] C. D. Ager and H. P. Hughes, *Optical Properties of Stratified Systems including Lamellar Gratings*, *Phys. Rev. B* **44**, 13452 (1991).
- [60] M. G. Moharam, D. A. Pommet, E. B. Grann, and T. K. Gaylord, *Stable Implementation of the Rigorous Coupled-Wave Analysis for Surface-Relief Gratings: Enhanced Transmittance Matrix Approach*, *J. Opt. Soc. Am. A* **12**, 1077 (1995).
- [61] Y. M. Lyaschuk, S. M. Kukhtaruk, V. Janonis, and V. V. Korotyeyev, *Modified Rigorous Coupled-Wave Analysis for Grating-Based Plasmonic Structures with a Delta-Thin Conductive Channel: Far- and Near-Field Study*, *J. Opt. Soc. Am. A* **38**, 157 (2021).
- [62] See Supplemental Material at <http://link.aps.org/supplemental/10.1103/PhysRevX.13.041003> for the technical details of the calculations and terahertz spectra fitting.
- [63] M. E. Levinshtein, S. L. Rumyantsev, and M. S. Shur, *Properties of Advanced Semiconductor Materials: GaN, AlN, InN, BN, SiC, SiGe* (Wiley, New York, 2001).
- [64] A. Tarekegne, B. Zhou, K. Kaltenecker, K. Iwaszczuk, S. Clark, and P. U. Jepsen, *Terahertz Time-Domain Spectroscopy of Zone-Folded Acoustic Phonons in 4H and 6H Silicon Carbide*, *Opt. Express* **27**, 3618 (2019).
- [65] W. Knap, E. Borovitskaya, M. Shur, L. Hsu, W. Walukiewicz, E. Frayssinet, P. Lorenzini, N. Grandjean, C. Skierbiszewski, P. Prystawko *et al.*, *Acoustic Phonon Scattering of Two-Dimensional Electrons in GaN/AlGaIn Heterostructures*, *Appl. Phys. Lett.* **80**, 1228 (2002).
- [66] P. Lorenzini, Z. Bougrioua, A. Tiberj, R. Tauk, M. Azize, M. Sakowicz, K. Karpierz, and W. Knap, *Quantum and Transport Lifetimes of Two-Dimensional Electrons Gas in AlGaIn/GaN heterostructures*, *Appl. Phys. Lett.* **87**, 2140880 (2005).
- [67] W. Knap, C. Skierbiszewski, K. Dybko, J. Łusakowski, M. Siekacz, I. Grzegory, and S. Porowski, *Influence of Dislocation and Ionized Impurity Scattering on the Electron Mobility in GaN/AlGaIn Heterostructures*, *J. Cryst. Growth* **281**, 194 (2005).
- [68] V. V. Korotyeyev, V. A. Kochelap, V. V. Kaliuzhnyi, and A. E. Belyaev, *High-Frequency Conductivity and Temperature Dependence of Electron Effective Mass in AlGaIn/GaN Heterostructures*, *Appl. Phys. Lett.* **120**, 252103 (2022).
- [69] Ben Yu-Kuang Hu and K. Flensberg, *Electron-Electron Scattering in Linear Transport in Two-Dimensional Systems*, *Phys. Rev. B* **53**, 10072 (1996).
- [70] W. L. Schaich, *Analysis of a Special Model for a Grating Coupler*, *Phys. Rev. B* **62**, 2721 (2000).
- [71] T. L. Zinenko, A. Matsushima, and A. I. Nosich, *Surface Plasmon, Grating-Mode and Slab-Mode Resonances in the h- and e-Polarized THz Wave Scattering by a Graphene Strip Grating Embedded into a Dielectric Slab*, *IEEE J. Sel. Top. Quantum Electron.* **23**, 1 (2017).
- [72] G. Cywiński, I. Yahniuk, P. Kruszewski, M. Grabowski, K. Nowakowski-Szkudlarek, P. Prystawko, P. Sai, W. Knap, G. Simin, and S. Rumyantsev, *Electrically Controlled Wire-Channel GaN/AlGaIn Transistor for Terahertz Plasma Applications*, *Appl. Phys. Lett.* **112**, 133502 (2018).
- [73] P. Sai, D. But, I. Yahniuk, M. Grabowski, M. Sakowicz, P. Kruszewski, P. Prystawko, A. Khachapuridze, K. Nowakowski-Szkudlarek, J. Przybytek, P. Wiśniewski, B. Stonio, M. Słowikowski, S. Rumyantsev, W. Knap, and G. Cywiński, *AlGaIn/GaN Field Effect Transistor with Two Lateral Schottky Barrier Gates towards Resonant Detection in Sub-mm Range*, *Semicond. Sci. Technol.* **34**, 024002 (2019).
- [74] D. Pashnev, V. Korotyeyev, J. Jorudas, A. Urbanowicz, P. Prystawko, V. Janonis, and I. Kašalynas, *Investigation of Electron Effective Mass in AlGaIn/GaN Heterostructures by THz Spectroscopy of Drude Conductivity*, *IEEE Trans. Electron Devices* **69**, 3636 (2022).